nature reviews methods primers

https://doi.org/10.1038/s43586-024-00293-8

Primer

Check for updates

X-ray diffraction under grazing incidence conditions

Oliver Werzer [1], Stefan Kowarik [2], Fabian Gasser [3], Zhang Jiang [4], Joseph Strzalka [4], Christopher Nicklin [5] & Roland Resel [3]

Abstract

Material properties frequently relate to structures at or near surfaces, particularly in thin films. As a result, it essential to understand these structures at the molecular and atomistic levels. The most accurate and widely used techniques for characterizing crystallographic order are based on X-ray diffraction. When dealing with thin films or interfaces, standard approaches, such as single crystal or powder diffraction, are not suitable. However, X-ray diffraction under grazing incidence conditions can provide the required information. In this Primer, grazing incidence X-ray diffraction (GIXD) is comprehensively introduced, starting from basic considerations on X-ray diffraction at crystals with reduced dimensionality and the optical properties of X-rays, followed by a more in-depth description of an experimental performance, including X-ray sources, goniometers and detectors. Experimental errors, limitations and reproducibility are discussed. Various applications, from highly ordered inorganic single crystal surfaces to weakly ordered polymer thin films, are presented to illustrate the potential of GIXD. Data visualizations, representations and evaluation strategies are summarized, based on the example of anthracene thin films. The Primer compiles information relevant to perform high-quality GIXD experiments, evaluate data and interpret results, to extend knowledge about X-ray diffraction from surfaces, interfaces and thin films.

Sections

[1]Joanneum Research Forschungsgesellschaft mbH — Materials, Weiz, Austria. [2]Department of Physical Chemistry, Institute of Chemistry, University of Graz, Graz, Austria. [3]Institute of Solid State Physics, Graz University of Technology, Graz, Austria. [4]X-Ray Science Division, Argonne National Laboratory, Argonne, IL, USA. [5]Diamond Light Source, Harwell Science and Innovation Campus, Didcot, UK. e-mail: roland.resel@tugraz.at

Introduction

X-ray diffraction is a valuable tool for material characterization, providing a large amount of knowledge about how atoms and molecules are arranged in matter. Most commonly, crystallographic information is obtained by structure solution from single crystals[1,2] and analysis of polycrystalline powders[3]. To investigate structures at surfaces or in thin films, various methods have been developed, for instance, spatially resolved microscopy techniques with atomic resolution[4,5]. Additionally, several X-ray techniques are available which are of integral character so that average information over extended sample areas is obtained. One method of probing surfaces and amorphous or crystalline thin films is X-ray reflectivity[6,7]. To reveal thin film morphologies, the surface structures – including feature size, shape and porosity[8–10] – of disordered and periodic structures, grazing incidence small-angle X-ray scattering (GISAXS) can be used. X-ray diffraction under grazing incidence conditions enables the crystalline features of surfaces and thin films to be accessed[11,12]. Structures are probed based on crystalline lattices and on the periodicity of atomic arrangements. Embedded crystallographic order within multilayer structures can be resolved, even at buried interfaces[13], providing a deeper understanding of semiconductor stacks[14,15] or functional organic layers[16–18]. Advantages of grazing incidence X-ray diffraction (GIXD) include no extensive sample preparation; applicability to gaseous, liquid and vacuum environments; and fast acquisition speeds that can study operando processes at surfaces[19].

This Primer focuses on the study of crystallographic properties of thin films and surfaces obtained under grazing incidence of an X-ray beam by wide-angle scattering. Using this geometry, atomic-scale information about the internal structure is required. Many different terms have been used to describe this technique. Examples include surface X-ray diffraction and grazing incidence wide-angle X-ray scattering (GIWAXS), with abbreviations such as GID and GIXRD also used in the literature. Throughout this article, the term 'grazing incidence X-ray diffraction' (GIXD) is used. The technique of GISAXS[8–10], which investigates structures on larger length scales, will not be discussed.

Theoretical background

This section introduces X-ray diffraction, with a focus on how to take the crystal shape into account, followed by the optical properties of X-rays when interacting with materials. Combining these two topics, the characteristics of GIXD are explored for crystallographic analysis of thin films and surfaces.

X-ray diffraction at thin films and surface lattices. X-ray diffraction is based on elastic scattering of X-rays, preferably on electrons, by a coherent scattering process, known as Thomson scattering[20]. To describe diffraction experiments, wave vector notation can be applied[21]. Using this notation, the geometry is defined by the wave vectors of the primary X-ray beam $\vec{k}_i$ and diffracted beam $\vec{k}_f$. These two vectors describe the direction of both X-ray beams. The length of the vectors relates to the energy, or wavelength λ, of the radiation. The central quantity of a diffraction experiment is the scattering vector $\vec{q}$, defined by the vector difference:

$$\vec{q} = \vec{k}_f - \vec{k}_i \text{ with } |\vec{k}_i| = |\vec{k}_f| = \frac{2\pi}{\lambda} \quad (1)$$

In kinematic diffraction theory, a diffraction peak that appears due to elastic X-ray scattering of the primary X-ray beam on the three-dimensional (3D) periodic lattice of a crystal is given by the Laue condition:

$$\vec{q} = \vec{G}_{hkl} \quad (2)$$

where $\vec{q}$ is the experimental quantity (Eq. 1) and $\vec{G}_{hkl}$ are discrete vectors within the reciprocal lattice, given by:

$$\vec{G}_{hkl} = h\vec{a}^* + k\vec{b}^* + l\vec{c}^* \quad (3)$$

where h, k and l are integers and $\vec{a}^*$, $\vec{b}^*$ and $\vec{c}^*$ represent the unit cell vectors of the reciprocal lattice. The connection between the real space lattice of $\vec{a}$, $\vec{b}$ and $\vec{c}$ and the reciprocal space vectors $\vec{a}^*$, $\vec{b}^*$ and $\vec{c}^*$ is given by a scaled vector cross product[22]. A useful relationship between the real and reciprocal space is shown in Fig. 1a. Crystallographic planes described by the Miller indices h, k and l and $\vec{G}_{hkl}$ are related, as the vector is perpendicular to the plane (hkl), with length $G_{hkl} = \frac{2\pi}{d_{hkl}}$, where d_{hkl} is the interplanar distance of the (hkl) planes.

The intensity of the diffraction peak $I(\vec{q})$ is related to two factors: the form factor $S(\vec{q})$ and the structure factor $F(\vec{q})$:

$$I(\vec{q}) \propto S(\vec{q}) \cdot |F(\vec{q})|^2 \text{ with } F(\vec{q}) = \sum_j f_j e^{i\vec{q}\vec{r}_j} \quad (4)$$

The structure factor $F(\vec{q})$ depends on the ability of individual atoms – denoted by the index j – to scatter X-rays, based on the atomic scattering factor f_j, and their relative position within the crystallographic unit cell $\vec{r}_j$. $S(\vec{q})$ represents the 3D Fourier transform of the investigated crystal lattice, which is related to the crystal size and shape. Assuming an infinite extended crystal lattice, a 3D Fourier transform represents the ideal reciprocal lattice[23] described by Eq. 3. For crystals with a limited size, the Fourier transform represents a specific function, with maxima at the reciprocal lattice points.

In a subsequent step, the specific shape of the form factor is considered for thin film crystallites and crystal surfaces. Variations from the infinite crystal extension are calculated perpendicular to the sample surface, denoted as the z axis in Fig. 1. By assuming that crystals are formed by a limited number of layers assembled by crystallographic unit cells, the form factor can be represented by the slit interference function[7,24]. Figure 1b shows a crystal formed by four layers of unit cells. The form factor shows the main peaks, with maxima at the initial q_z (or G_{hkl}) positions of the reciprocal lattice points. Additionally, several side peaks are present. The peak width of the main maxima Δq_z relates to the crystal extension L_z by:

$$L_z \approx \frac{2\pi}{\Delta q_z} \quad (5)$$

often referred to as the Scherrer formula[25]. The side maxima are called Laue oscillations[26].

A limiting case is a pure two-dimensional (2D) lattice, with the geometric relationship shown schematically in Fig. 1c, where the form factor represents straight lines in the reciprocal space along the z direction, referred to as Bragg rods[27]. Bragg rods can only be observed when the structure factor $F(\vec{q})$ is sufficiently large for the resulting intensity $I(\vec{q})$ to be detectable (Eq. 4).

A specific form factor can be found by considering a theoretical infinite crystal lattice with a missing upper half. Cleaving of a crystal produces a flat surface – an x,y plane – to obtain a crystal with a missing

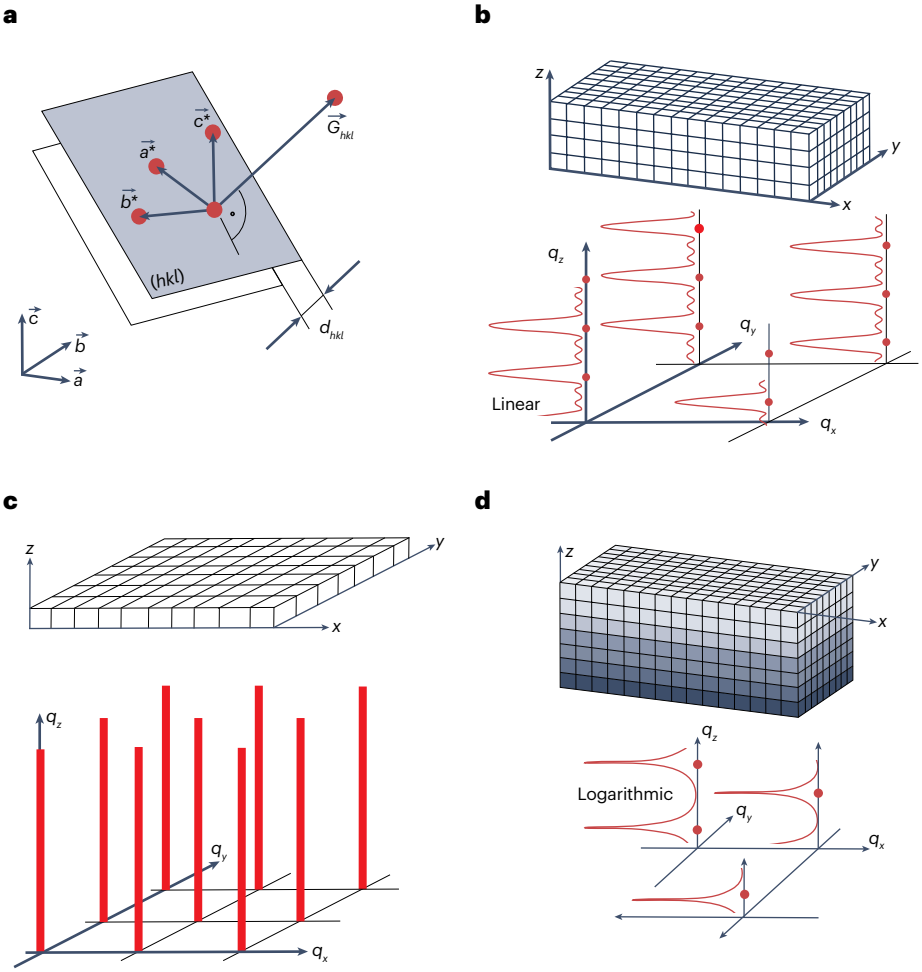

Fig. 1 | Real space crystal lattices and their reciprocal space representations. a, Correlation between the real space lattice (spanned by $\vec{a}, \vec{b}, \vec{c}$) and the reciprocal space lattice ($\vec{a}^*, \vec{b}^*, \vec{c}^*$) via the reciprocal lattice vector $\vec{G}_{hkl}$ and the crystallographic plane (*hkl*) with the interplanar distance d_{hkl}. Reciprocal lattice points are given by red spots. **b**, A size-limited crystal with four layers of crystallographic unit cells together with the resulting form factor along the q_z direction. **c**, A two-dimensional (2D) crystal lattice together with the representation in the reciprocal space by Bragg rods (red vertical bars). **d**, A cleaved crystal with a defined surface causes, in reciprocal space, a finite function between the reciprocal lattice points denoted as crystal truncation rods (CTRs). *h*, *k*, *l*, Miller indices; q_x, q_y, q_z, reciprocal space coordinates (reciprocal lattice points as full red dots); *x*, *y*, *z*, real space coordinates.

top half-space (only lattice points with $z \leq 0$ remain). The Fourier transform gives finite functions between the reciprocal lattice points of the original infinite lattice[7]. An example is plotted with the real space picture of the truncated crystal in Fig. 1d. The intensity distribution in the *z* direction across the reciprocal lattice points is called the crystal truncation rod (CTR)[7,28].

Optical properties of X-rays interacting with matter. The refractive index *n* describes how the primary X-ray beam behaves when interacting with the sample (Fig. 2a). The beam phase and propagation direction change when different materials are involved, as described by Snell's law[7]. The refractive index can be obtained by following formulas, but these are not valid close to an absorption edge[29]:

$$n \equiv 1 - \delta + i\beta \text{ with } \delta = \frac{\lambda^2}{2\pi} r_e \rho_e \text{ and } \beta = \frac{\lambda}{4\pi}\mu \quad (6)$$

The refractive index decrement δ and absorption β depend on the X-ray energy *E* (or wavelength λ), the total electron density ρ_e of the sample material and the sample's linear absorption coefficient μ[30,31]. The classical electron radius r_e is equal to 2.81794×10^{-15} m. Typically, δ ranges from 10^{-5} to 10^{-6} and β from 10^{-7} to 10^{-8}, with characteristic values presented in Table 1. As the refractive index of matter is slightly smaller than 1 — for air the value is very close to 1 — total external reflection of X-rays at the sample surface can occur at an angle of grazing incidence α_i smaller than the material-dependent critical angle of total external reflection α_c. The refractive indices for matter, air and vacuum are close, resulting in small critical angles that can be determined by:

$$\alpha_c = \sqrt{2\delta} \quad (7)$$

The Fresnel equations describe the angle-dependent intensities of the beam reflected from and penetrating into the sample surface[32,33]. An important quantity is the penetration depth Λ of the penetrating wave into a flat sample. This defines the characteristic length — perpendicular to the sample surface — to decrease the X-ray beam intensity by a factor 1/e. At large incidence angles, Λ results from the sample's linear absorption coefficient μ. At incidence angles below α_c, there is limited penetration due to total external reflection ($\alpha_i < \alpha_c$). Figure 2b shows angle-dependent examples of the characteristic penetration depths for gold, silicon and anthracene, which have different electron densities ρ_e (Table 1). Below α_c, Λ is a few nanometres. As a result, GIXD is controllable and sensitive to surface information, enabling bulk information to be excluded when needed. Moreover, α_i can be varied to characterize the crystallographic structure at defined depths from the surface.

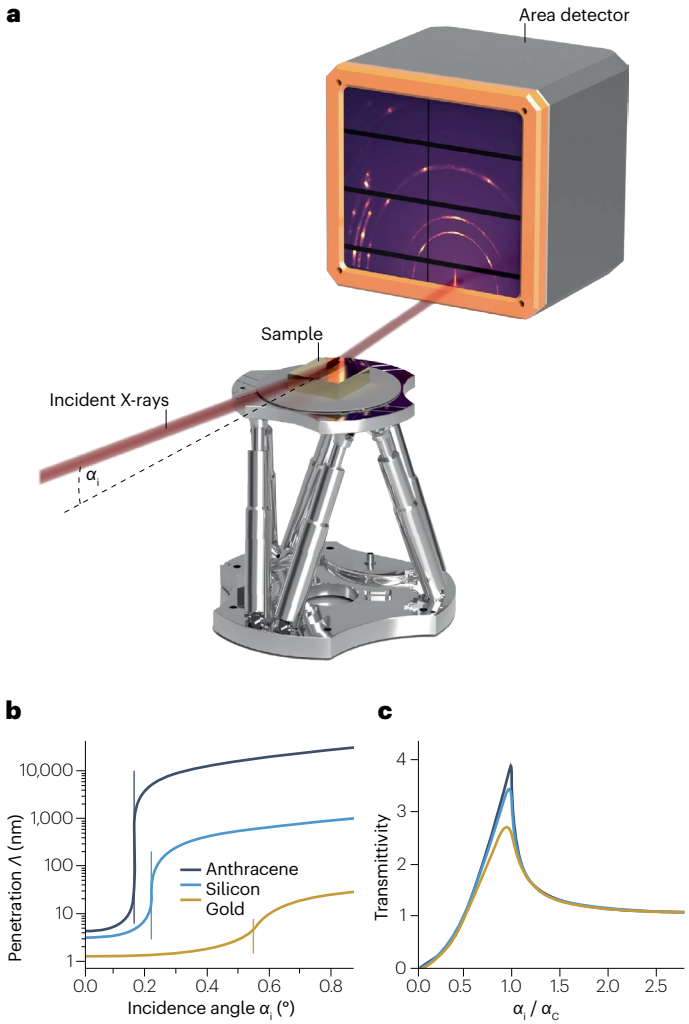

Fig. 2 | Optical properties of the primary X-ray beam. a, Experimental set-up including the X-ray beam, the manipulation stage hosting the sample and a detector. An important parameter for grazing incidence X-ray diffraction (GIXD) experiments is the angle of grazing incidence α_i relative to the sample surface. **b**, Material-dependent penetration depth Λ as a function of α_i. Critical angles given by vertical lines. **c**, Transmittivity, or normalized evanescent wave intensity, as a function of the ratio between α_i and the critical angle of total external reflection α_c.

The transmitted wave can be described as an evanescent wave because exponential decay of the X-ray intensity occurs in the region of total external reflection. The normalized intensity of this wave — the transmittivity[7,34] — is shown in Fig. 2c as a function of the incidence angle. Considerable enhancement of the transmitted, or evanescent, wave intensity is observed at the critical angle ($\alpha_i = \alpha_c$), up to a factor of four[35]. This enhancement is due to the incoming and reflected beams adding up in phase, leading to twice the scattering amplitude or four times the intensity, and is crucial for studying thin layers as it increases the signal-to-noise ratio.

A related optical effect is the Yoneda peak[36]. Alongside the intensity enhancement when $\alpha_i \approx \alpha_c$, enhanced intensity is also observed under the condition $\alpha_f \approx \alpha_c$, where α_f is the angle between the reflected X-ray beam and the sample surface.

Combining optical properties of X-rays with diffraction. GIXD is based on the concept that the transmitted X-rays (Fig. 2c) are diffracted on periodic lattices within the penetration depth Λ, located at the sample surface for $\alpha_i \leq \alpha_c$ or close to the surface for $\alpha_i \geq \alpha_c$[34,37].

The 2D lattices can be studied by selecting a wave vector for the primary beam and diffracted beam parallel to the sample surface, by using $\alpha_i \approx \alpha_c$ and $\alpha_f \approx \alpha_c$[38]. The resulting scattering vector (Eq. 1) is aligned in-plane, parallel to the sample surface. By varying the length and direction of the scattering vector, the q_x and q_y positions of the Bragg rods can be found by detecting enhanced intensity (Fig. 1c). Intensity distributions along Bragg rods — at a defined q_x, q_y position but with varying q_z — can be determined by arranging the wave vectors $\vec{k}_i$ and $\vec{k}_f$ accordingly. A similar approach is used to study the intensity distribution along CTRs. The large intensity distribution over several orders of magnitude along the CTR means that experimental results are usually presented on a logarithmic scale to highlight modulations in the profile (Fig. 1d).

Crystalline properties of thin films can be investigated based on diffraction peaks at defined values of q_x, q_y and q_z. Using a grazing incidence condition ($\alpha_i \approx \alpha_c$) for the primary X-ray beam, a large variety of different scattering vector lengths and directions can be accessed. However, there is an inaccessible region located at $q_x = q_y = 0$ along the q_z coordinate. The term missing wedge is used to describe the specific volume within the reciprocal space that cannot be covered in a GIXD experiment with a single incidence angle. In summary, different measurement strategies are available to observe diffraction peaks, depending on the distribution of the crystallites — referred to as texture — within the sample. By monitoring diffraction peaks in reciprocal space, the crystallographic texture can be revealed. Using GIXD, analysis of the crystalline properties based on peak positions, peak widths and peak shifts can be determined.

Main achievements

GIXD has developed into a powerful method. Originally, periodic surface reconstructions[27,39–41] and 2D crystals[42–44] were studied extensively. With the realization that many phenomena are driven by surface and interfacial effects, a wider range of GIXD applications emerged. As a consequence, thin films are studied on a regular basis. Phase analysis[45], preferred orientation of crystals[46], epitaxial order[47], depth-dependent information[48] and order at buried interfaces[49] are commonly investigated[50]. Using intense synchrotron radiation, in situ studies of film formation can be performed to determine growth kinetics, phase transitions and transient structures[51,52], phase changes induced by temperature or solvents[53] and catalytic reactions[54].

Experimentation

GIXD experiments are performed using a wide range of diffractometer and detector set-ups in both laboratories[55–57] and synchrotrons[58–65]. To obtain accurate and meaningful results, it is essential that experimental set-ups are optimized considering the characteristics of each sample system. For example, samples can exhibit weak scattering as observed for molecular materials[44], require high resolution for highly perfect crystals[62] or need the incident beam to be bent vertically downwards for liquid surfaces that cannot be tilted[62,63,66]. Additionally, the sample environment must be considered, for instance to measure the sample as a function of temperature[67], in vacuum during thin film deposition[68–70], in a gaseous or solvent atmosphere[71], or in liquids for electrochemical investigations[72,73]. A detailed discussion of each environment is not

possible and, as a result, this section focuses on the basic GIXD experimental requirements. Grazing incidence diffraction experiments are also performed using neutrons[10,74,75] or electrons[76–78] and each type of radiation has its own limitations.

Experiments with the highest data quality are conducted at synchrotron facilities and each has a unique set-up and capabilities. Examples include dedicated surface diffraction beamlines at Elettra[79], ESRF[63,80], PETRA III/DESY[62], ALBA (BL11), CHESS (QM2), DIAMOND[81], SOLEIL[59], SPring-8 (refs. 60,61,82), SSRF[83], SLS[84,85], CLS (Brockhouse), APS[64], ALS[86], NSLS-II[65] and SSRL (BL1-5, BL2-1). Laboratory-based diffractometers are being increasingly used, such as the Bruker DISCOVER[55], Rigaku Smartlab or Panalytical Empyrean. Additionally, instruments marketed for SAXS applications — such as the Anton Paar SAXSpace or Xenocs Xeus — can often be adapted for GIXD by moving the detector close to the sample.

Once the sample and sample environment have been defined, an optimized X-ray scattering geometry can be devised. The resulting diffraction set-ups encompass different primary beam shapes and focus positions, offering various degrees of freedom and options to align the set-up with other components. The choice of detector and collimation system is also crucial for angular and time resolution (Fig. 3a).

Primary X-ray beam requirements

To ensure high-quality data acquisition with sufficient signal-to-noise ratio and resolution, several criteria must be met by the primary X-ray beam. Diffraction signals from (ultra-)thin films can be weak, often eight orders of magnitude less than the primary beam. Although the diffracted beam is enhanced at the critical angle (Fig. 2c), sufficient beam flux and intensity is crucial for obtaining reliable results and keeping counting times reasonably low. Another important issue is the vertical beam size when using a horizontal sample orientation. As shown in Fig. 3b, the illuminated length of a beam will usually extend beyond the sample. For example, an X-ray beam with a 100 µm vertical size at an incident angle $\alpha_i = 0.1°$ will illuminate nearly 60 mm at the sample surface, referred to as the beam footprint. As a result, only a fraction of the beam contributes to diffraction from a sample of limited extension. Vertical beam focusing, or beam compression, reduces the beam footprint while increasing the photon flux on the sample to enhance the GIXD signal, albeit at the risk of beam damage.

By contrast, the horizontal beam size has a secondary influence on resolution in real and reciprocal space, as indicated by the extended parallelogram shape of the diffracted beam in Fig. 3c. Extension of the measured Bragg reflection on an area detector is mainly influenced by the horizontal beam dimension at lower angles. At larger scattering angles — further away from the primary beam — the sample size or X-ray beam footprint becomes a determining factor in defining the apparent Bragg reflection size. The image on the detector shown in Fig. 3c is only a schematic representation of a GIXD signal, as there are usually more reflections from CTRs; however, the indicated parallelogram shape will apply to all reflections. To minimize the experimental impact on peak width, high-resolution measurements are required, with careful consideration of the beam properties and detector. Specifically, the beam should have low divergence to minimize smearing of Bragg reflections. Beam divergence can blur the diffraction pattern, affecting the resolution. Scattering at beam shaping slits and background from air scattering should be minimized, especially if measurements at low q values are of interest. In summary, a well-optimized primary X-ray beam must satisfy multiple criteria, including sufficient intensity, appropriate vertical beam size and low divergence.

Detectors and collimation systems

Different detectors have been developed, with each new generation providing improvements in noise, number of pixels per area, dynamic range or read-out rates. Many experimental set-ups, especially at synchrotrons, have a choice of detector systems or can use multiple detectors simultaneously to record several regions in reciprocal space. The sample dictates the choice, depending on the desired data quality and measurement speed. A commonly used set-up involves an area detector, such as a photon counting detector with high dynamic range[87]. This type of detector enables large GIXD patterns to be collected in a specific α_f/θ_f range in a single shot, with a resolution limited by the detector pixel density. In practice, the geometric projection of the beam profile (Fig. 3c), not the pixel size, often limits the resolution. For single crystals, epitaxial films or films with biaxial texture, the sample rotates along θ_i, which combined with θ_f and α_f scans could take a prohibitively long time. The high acquisition speed of GIXD with area detectors enables large volumes of reciprocal space to be inspected and angular variation, which is required for rotating GIXD, is more feasible.

Area detectors are usually used without collimation and the background scattering signal can overshadow weak Bragg reflections. Air scattering, diffraction from the sample holder, windows in the beam path and X-ray fluorescence excited by the primary beam can contribute to features and background on the detector image. As this background has a complicated structure, it cannot be subtracted reasonably well. Slits before the sample and a beam stop after the sample can help reduce air scatter. 3D-printed radial collimators have been successfully demonstrated to reduce background in GIXD with area detectors[88].

Point detectors and linear position-sensitive detectors were used before area detectors were developed. These detectors continue to be used, as they have higher resolution and lower background scattering due to extended collimation systems. For point detectors, such as scintillation counters, two slit pairs define a small volume from which diffraction is measured (Fig. 3a). A mesh scan measures all points in the $\theta_i/\alpha_f/\theta_f$ space. This is time consuming both with integration times of minutes per point on laboratory diffractometers and for integration times of seconds per point at synchrotron light sources. Often, only a scan at a defined θ_i value is performed, or a specific CTR or Bragg rod (Fig. 1c,d) is followed in the q_z direction. In a horizontal sample

Table 1 | Values of various parameters used to calculate the optical properties of X-rays (such as penetration depth and transmittivity) of gold, silicon and the molecular material anthracene

	ρ_e (Å^{-3})	E (keV)	δ	α_c (°)	μ (cm^{-1})	β
Anthracene	0.408	8	4.27×10^{-6}	0.170	5.32	6.56×10^{-9}
Silicon	0.712	8	7.67×10^{-6}	0.224	143	1.77×10^{-7}
Gold	4.43	8	4.77×10^{-5}	0.560	4013	4.95×10^{-6}

α_c, critical angle of total external reflection; β, absorption part of the refractive index; δ, dispersive part of the refractive index; E, energy of X-rays used to calculate the presented values for the optical parameters; ρ_e, average electron density including all electrons of the material; μ, linear absorption coefficient.

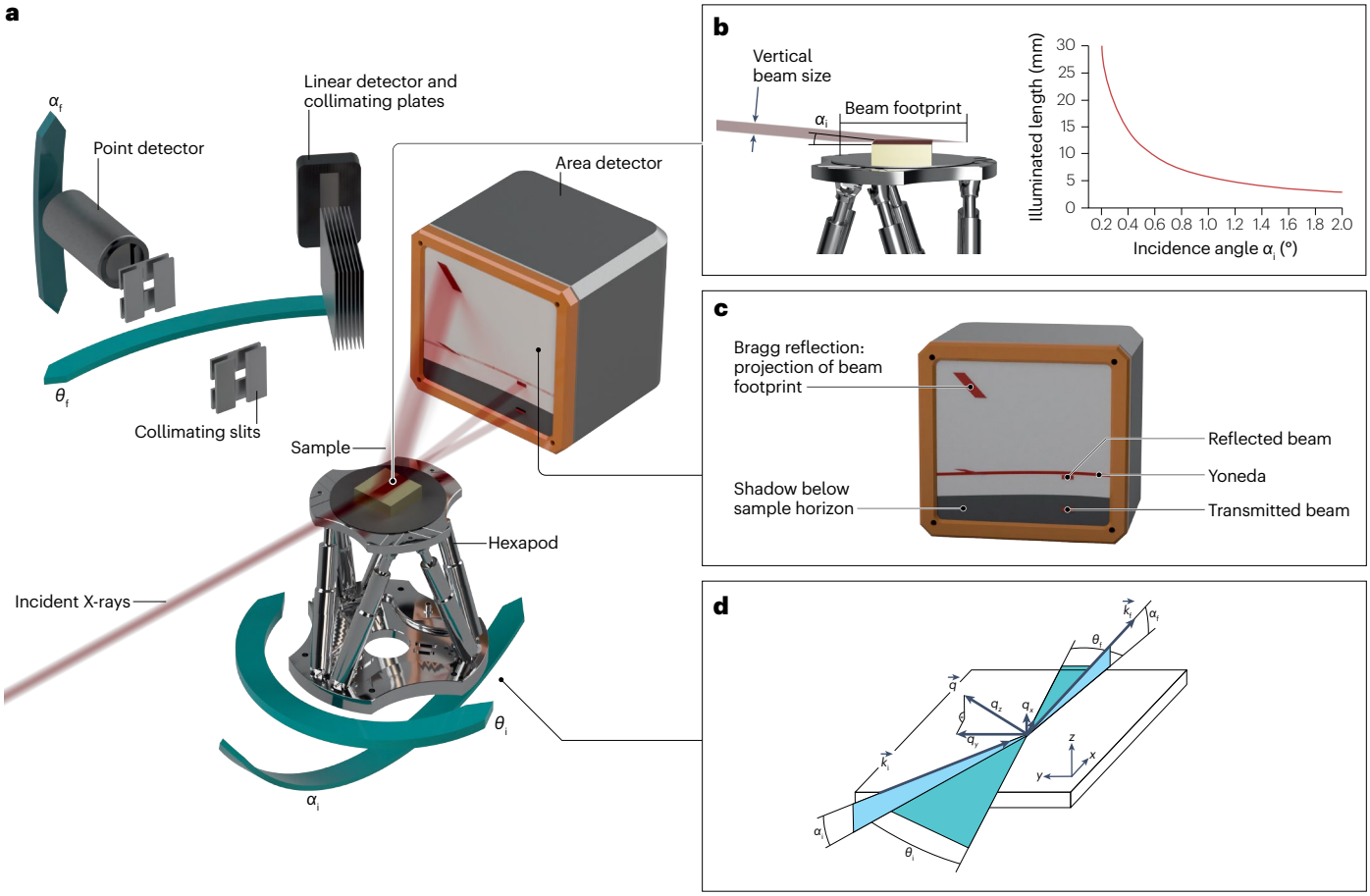

Fig. 3 | Experimental set-ups of a grazing incidence X-ray diffraction (GIXD) experiment. a, Incident X-ray beam with the sample placed on a hexapod for alignment purposes together with the incidence beam angles θ_i and α_i. The system for detection of the diffracted beam can be either an area detector, a linear detector or a point detector. The latter two must be scanned along the diffraction angle θ_f (linear detector) or along both angles θ_f and α_f (point detector). The collimation systems are plate collimators for a linear detector or slit systems for point detectors. **b**, Footprint of the primary beam at the sample surface depending on the incident angle α_i. **c**, Different shapes of the diffracted X-ray beams at the detector. **d**, Beam geometry with $\vec{k}_i$ and $\vec{k}_f$ as the wave vectors of the primary and the scattered X-ray beam together with the scattering vector $\vec{q}$ separated into its components q_x, q_y and q_z according to the sample coordinate system x, y, z. Angular movements are used to position the samples in real space coordinates. α_f, angle between the reflected X-ray beam and the sample surface; α_i, angle of grazing incidence.

geometry, vertical slits in front of the point detector are sometimes opened wide to ensure that the sample horizon and enhanced Bragg reflections in the Yoneda region are not obstructed in a simple in-plane θ_f scan. A more efficient way to acquire GIXD patterns is with a linear detector[55]. These detectors can be used in conjunction with relatively large plate collimators, as shown in Fig. 3a, which eliminates a large portion of unwanted scatter and fluorescence[55]. The resolution in the in-plane direction is high, but as the plates are open in the vertical direction there is smearing along q_z.

In contrast to experiments with monochromatic illumination and detection, some studies use an energy dispersive detector with a white or pink primary X-ray beam, which has a continuous wavelength spectrum[89–91]. However, the current generation of energy dispersive detectors has limited dynamic range. Additionally, the underlying principles make it challenging to capture very small and very large q values at the same time in the limited energy bandwidth of a single white X-ray beam exposure.

Goniometer requirements

The sample needs to be accurately positioned and aligned with respect to the primary X-ray beam. Positioning is assisted by goniometers, typically consisting of rotational and translational actuators. During an experiment, best practice is to position the sample surface in the rotation centre of the goniometer. It is therefore crucial to have sufficient degrees of freedom within the goniometer. For some experimental stations only limited freedom exists, whereas others might have multiple translation and rotation options. Hexapods, as depicted in Figs. 2a and 3a,b, are an elegant possibility for sample alignment in terms of tilting, azimuthal rotation and x–y–z translational movement.

Sample alignment enables precise determination of angles relevant to the diffraction experiment[92] (Fig. 3d). The angles α_i and θ_i define the direction of $\vec{k}_i$ (primary wave vector) relative to the sample surface, whereas the angles α_f and θ_f define $\vec{k}_f$ (diffracted wave vector). α_i and α_f are angles relative to the sample surface, but θ_i and θ_f are angles relative to the x axis of the sample coordinate system. The scattering

vector $\vec{q}$ is the difference of both wave vectors and is the quantity of interest. The three directional components q_x, q_y and q_z of the scattering vector in sample coordinates derive from basic geometrical equations:

$$q_x = \frac{2\pi}{\lambda}(\cos\alpha_f\cos\theta_f - \cos\alpha_i\cos\theta_i)$$

$$q_y = \frac{2\pi}{\lambda}(\cos\alpha_f\sin\theta_f - \cos\alpha_i\sin\theta_i) \quad (8)$$

$$q_z \cong \frac{2\pi}{\lambda}(\sin\alpha_f + \sin\alpha_i)$$

A refraction correction must be taken into account for exact calculation of q_z, especially if α_i and/or α_f is chosen close to α_c[29,38]. The length of the scattering vector (not refraction corrected) can be related to the scattering angle 2θ, the angle between the primary and scattered beam, by:

$$|\vec{q}| = q = \frac{4\pi}{\lambda}\sin\frac{2\theta}{2} \quad (9)$$

During a GIXD experiment, the scattering vector is varied by adjusting the angles α_i, α_f, θ_i and θ_f according to Eq. 8, which provides information on the diffracted intensities at different q values. The variation strategy can be adapted for different samples. If no sample rotation in θ_i is required — for example, for a textured 2D powder sample — and if an area detector is used, no further scanning of θ_i and θ_f is needed during a single measurement. Using this approach, GIXD measurements are fast with integration times below 1 ms[93]. Other samples may require variation of α_i and θ_i to obtain all the necessary information. Variation of θ_i can be easily achieved by rotating the sample around its surface normal. This rotating GIXD method has a wide range of applications, including reduction of weak statistics for 2D powders and detailed inspection of highly defined samples, such as single crystals or epitaxially grown films.

Synchrotron experiments often exploit the in situ capabilities of GIXD. As a result, the diffractometer must be mechanically resistant to support potentially heavy sample environments, such as catalysis, heating[94,95] or thin film growth chambers[68]. This often leads to large diffractometers. New developments in manufacturing by mechanical machining and additive manufacturing provide the option of smaller sample environments, which are lighter and more cost-effective, expanding the range of possible set-ups.

Sample alignment and calibration

Sample alignment and calibration of the set-up are critical steps in GIXD experiments. To align the sample, various adjustment steps have to be made[96]. This includes nulling the roll and pitch of the sample, optimizing the sample height z and achieving adequate, lateral centring in the x and y directions. Height scans along the z direction are performed multiple times during the alignment procedure. These scans involve cutting the primary beam in half at a 0° incidence angle. Subsequently, the sample is rocked in the primary beam while observing the shadowing. This enables a rough alignment of the sample surface parallel to the X-ray beam. Fine adjustments of the pitch and roll are made by aligning the sample until the optically reflected beam at an incidence angle α_i in the range of 0.5–2° is correctly directed. The time required for a typical sample alignment procedure is in the range of minutes. Automation improves reproducibility and reduces the required time. Sample misalignment causes a shift of Bragg peak positions in the subsequent GIXD experiments[96].

The set-up angles result from geometrical considerations, but as uncertainties exist it is best practice to test the set-up using a calibration sample. This calibration process involves determination of the primary beam position at the detector, accurately measuring the sample–detector distance and correcting geometric distortions, especially when using a flat area detector. Calibration is typically performed using materials with well-known diffraction patterns and strong Bragg reflections of randomly distributed crystallites. Common calibration materials include lanthanum hexaboride (LaB_6), silicon, or silver behenate in a capillary or as a surface coating[97,98]. Defect-free single crystals, such as silicon wafers, can aid surface alignment, and calibration in rotating GIXD experiments.

Results

GIXD is highly versatile, with many data collection strategies depending on the sample of interest. Samples with randomly distributed crystals require the least experimental effort as the reciprocal lattice points of randomly oriented crystals arrange in spheres centred around the origin of the reciprocal lattice. A typical representation is depicted in Fig. 4Aa. Simple line scans using a point detector provide information for further crystallographic evaluation. Using an area detector, cutting through the spheres results in commonly centred circles, referred to as Debye–Scherrer rings (Fig. 4Ab). Homogeneous rings are observed from perfect powders, whereas weak randomness or poor statistics, which is typical for crystals with extended size, results in intensity variations along the.

When the orientational randomness in a powder reduces, the sample is textured. In thin films, the presence of a substrate can result in a defined crystallographic plane — the contact plane — parallel to the substrate surface. Thin films on isotropic substrates often have a random azimuthal direction, leading to 2D powders[99]. Other terms used for such samples are fibre textures[100] or uniplanar[101]. 2D powders have distinct scattering compared with randomly distributed crystallites because the reciprocal lattice points arrange into concentric rings (Fig. 4Ba) rather than spheres. Measurements at a fixed (azimuthal) sample alignment, by a linear or area detector, are sufficient to cut through the reciprocal space for data collection[45].

A further reduction in the crystal's orientational freedom occurs in uniaxially[101] or biaxially aligned crystals[102], typically for epitaxially grown films or single crystal surfaces. This leads to localized distributions of reciprocal lattice points in the reciprocal space. Consequently, a more demanding data collection strategy, similar to single crystal diffraction experiments, is required. The detector and sample need to be varied for diffraction to be recorded. When using rotating GIXD, an area detector is best. In this approach, images are taken at a fixed detector position and various azimuth sample positions (angle θ_i) so that the reciprocal lattice points intersect the detector plane[79].

Another type of sample is 2D crystals at surfaces and truncated crystals. Their reciprocal space representation are Bragg rods and CTRs, as depicted in Figure 1b,c. For measurements, line or area detectors are suitable; however, the intensity is localized, meaning exact azimuthal alignment of the sample with respect to θ_i is required.

Data reduction and representation

The collected data provide intensities at defined directions, for example, by pixels in an area detector. Several software packages for simple data visualization are provided by detector companies.

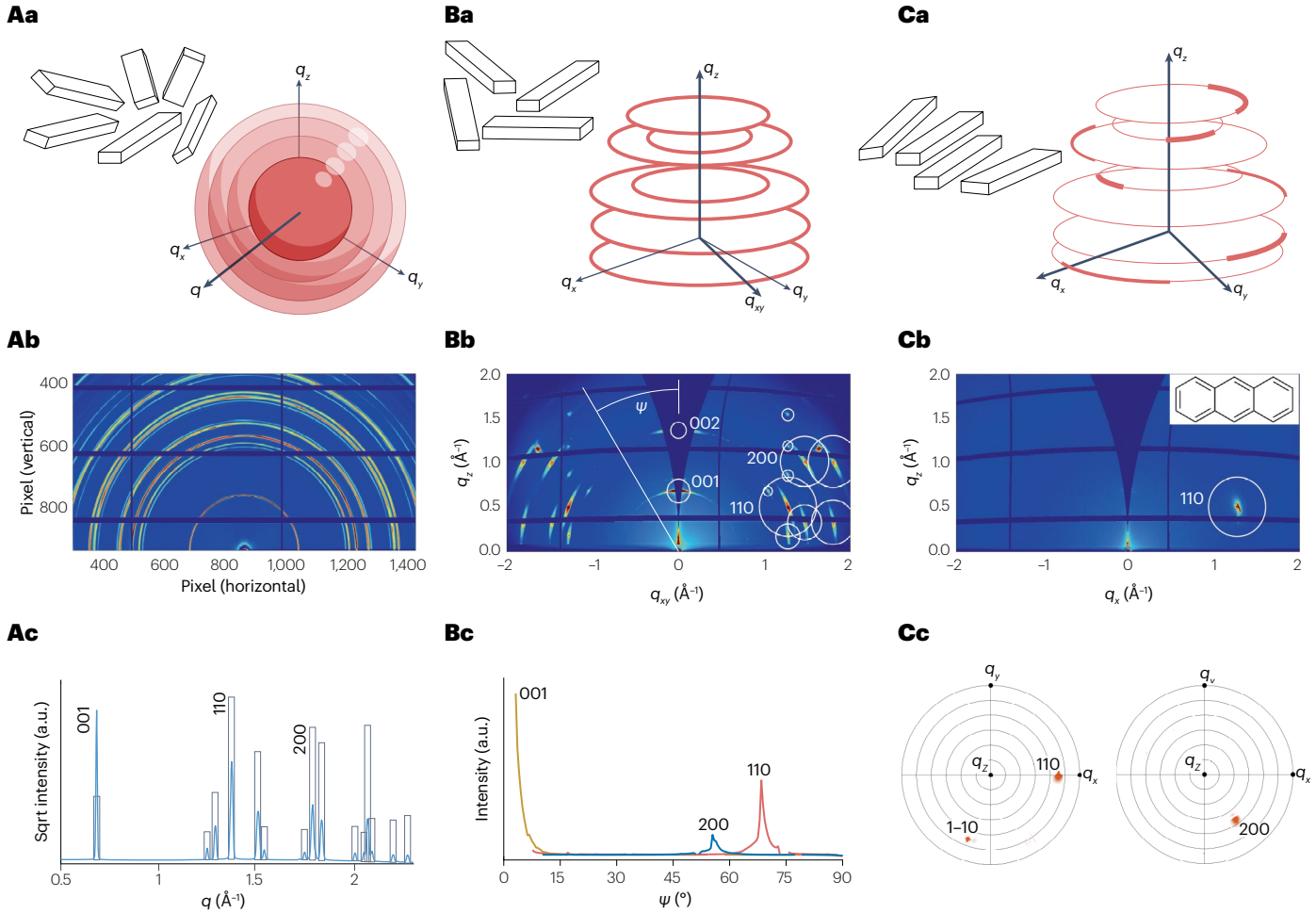

Fig. 4 | Types of thin film samples and exemplary results on anthracene. **Aa**, Randomly distributed crystals result in reciprocal lattice points assembled in concentric spheres. **Ab**, Real space detector image showing Debye–Scherrer rings. **Ac**, Powder plot in comparison with $|F_{hkl}|^2$. **Ba**, Uniplanar crystal orientation relative to the substrate surface results in reciprocal lattice points assembling in concentric circles parallel to the q_x, q_y plane. **Bb**, Corresponding reciprocal space map showing distinct spots; calculated peak positions and peak intensities represented by $|F_{hkl}|^2$ scaled circles. **Bc**, Radial intensity profiles evaluated at $q = 0.68$ Å^{-1}, 1.37 Å^{-1} and 1.78 Å^{-1} for 001, 200 and 110, respectively. **Ca**, Crystals with biaxial alignment with some mosaic spread of the reciprocal lattice points along a single azimuth direction. **Cb**, A separated Bragg peak as a function of a defined q_x, and q_z cut of the reciprocal space. **Cc**, Pole figures for the crystallographic planes (110) (taken at $q = 1.37$ Å^{-1}) and (200) ($q = 1.78$ Å^{-1}). Polar angle ψ indicated in steps of 15° by concentric circles; directions of reciprocal space coordinates q_x, q_y and q_z given by red dots.

More sophisticated data manipulation methods, such as calibration, are available from community-developed tools, including FIT2D, NeXpy, ImageJ, view.gtk[103–105] and the Python package xrayutilities[106]. Transferring experimental data from detector images into the reciprocal space representation has advantages. For example, it provides a wavelength-independent representation of the diffraction data, an angle-true representation of crystal directions or equidistant separations of Bragg peaks with their higher order reflections. The respective conversion formulae are given in Eqs. 8 and 9.

Various software packages have emerged[10], for example GIXSGUI[107] and GIDVis[108]. These provide data manipulation and representation so that they can be utilized for well-established evaluation of crystallographic properties[109,110]. The overall goal is to access as much information as possible about the sample, including crystallinity, type of crystal order, polymorph identification, crystal orientations, crystal size and microstrain or macrostrain.

Example studies on anthracene thin films

To show the variability of GIXD experiments, example studies on anthracene thin films are summarized in Fig. 4. The various films were prepared differently and are all polycrystalline but have different textures.

The first anthracene film is composed of randomly distributed crystallites, which results in arrangements of reciprocal lattice points along spheres (Fig. 4Aa). A collected detector image is presented in Fig. 4Ab. The black stripes are blind areas related to the construction of the detector. The detector image is transferred into angular space and reciprocal space based on the GIXD set-up calibration. In terms of

rings, one good possibility for data representation is to integrate the intensity along constant q values, along the rings, to produce a powder plot (Fig. 4Ac). Comparing the experimental peak positions and intensities with a known crystal structure of anthracene[111], there is a good agreement of position. Deviations in the relative peak intensities are resolved by applying geometrical correction factors.

The second anthracene example of a thin film has textured crystallites. All crystallites have one defined crystallographic plane parallel to the substrate surface but are randomly oriented in-plane as a 2D powder or uniplanar texture. The corresponding reciprocal lattice points are arranged along concentric circles (Fig. 4Ba). As a result, it is sufficient to collect diffraction data at a fixed sample orientation. Transfer of the original detector image into reciprocal space results in a distortion, which is noticeable in the dark horizontal and vertical stripes (Fig. 4Bb). The data are plotted as a function of the out-of-plane and in-plane part of the scattering vector, q_z and q_{xy}, respectively. For the latter, $q_{xy}^2 = q_x^2 + q_y^2$ is used. An alternative representation of the experimental data are radial pole figures. For the individual Bragg reflections of a given q value, the intensity distribution along the ring direction is plotted with the polar angle ψ as the coordinate of representation[57,112] (Fig. 4Bc).

The third anthracene example represents in-plane, or azimuthally, aligned crystallites. The corresponding reciprocal lattice points are along concentric circular segments (Fig. 4Ca). The data were collected using rotating GIXD. Single reciprocal space maps can be obtained by plotting the in-plane part of the scatting vector in a particular direction, such as q_x, as a function of q_z. A smaller number of diffraction peaks appear in this individual GIXD map (Fig. 4Cb) because the reciprocal lattice points are present only at limited azimuthal angles (Fig. 4Ca). Consequently, the Laue condition (Eq. 2) can be fulfilled only when the azimuths of the sample are chosen correctly. A specific type of data visualization is pole figures[113], as shown in Fig. 4Cc. Generally, pole figures are used to describe the texture of crystals. A single pole figure gives the orientation distribution of one defined crystallographic plane relative to the sample coordinates[114,115]. The poles, or net plane normal, are often presented in Eulerian angles.

Analysis and model fitting

Analysis of X-ray diffraction data is highly developed. Most of the well-established data evaluation techniques can be applied to GIXD data[109,110,114]. One outstanding advantage of GIXD is that it can be performed direction dependently, for instance in the out-of-plane direction or in-plane direction[46,116]. So crystallographic information can also be determined direction dependently. Additionally, GIXD enables information to be collected as a function of sample depth, to distinguish surface structures and deeply embedded structures[48].

GIXD experiments provide exact positions of Bragg peaks, which are related to the crystallographic lattice, relative to the sample coordinates. Applying orientation matrices[23,117] enables the crystalline real and reciprocal lattice to be rotated. As a result, calculated reciprocal lattice points can be brought into agreement with experimental observations to perform qualitative phase analysis and determine the preferred orientation[118]. In the example of anthracene, this is indicated by white rings centred around the Bragg peaks (Fig. 4Bb,Cb).

If the crystal phases are unknown, indexing of the GIXD pattern — assignment of Laue indices to the individual diffraction peaks — can identify the underlying crystal lattices. There are several approaches to index a GIXD pattern[47,119,120] and specific software solutions have been developed[121–123]. Comparison with databases — such as the Powder Diffraction File from the International Centre for Diffraction Data (ICDD) — or calculated patterns based on crystal structure information from a .cif file, enables clear identification of the phase present (Fig. 4Ac,Bb).

More detailed crystallographic analysis, for example, to derive information on atomic positions within the unit cell, requires the intensities of experimental Bragg peaks. Peak fitting or integration in a region of interest are performed. The intensities $I(q)$ are connected to the form factor $S(q)$ and to the square of the structure factors $F(q)$ (Eq. 4). Variation in the intensity results from experimental geometric factors[124]:

$$I(\vec{q}) = L(\vec{q}) \bullet P(\vec{q}) \bullet H_{hkl} \bullet A(\vec{q}) \bullet R(\vec{q}) \bullet Z(\vec{q}) \bullet D(\vec{q}) \bullet T(\vec{q}) \bullet S(\vec{q}) \bullet |F(\vec{q})|^2 \quad (10)$$

The most important factors are the Lorentz factor L[125], polarization factor P[126], peak multiplicities H_{hkl}, area factor A[127], detector efficiency correction Z[107], Debye–Waller factor D[7] and the transmitted wave intensity T, which differs from 1 at small q_z values[35]. The rod interception factor R[39] may play a role too. Most of these factors are also dependent on the scattering vector $\vec{q}$. Based on these geometric functions, quantification in terms of phase analysis or texture analysis can be performed[45]. A comparison of experimental intensities with the square of the structure factors is indicated by area of the circles (Fig. 4Bb) or by bars in powder plots (Fig. 4Ac).

Peak intensities are also required to access crystal orientation information in respect to the substrate. The mosaicity expresses the angular distribution of the crystals, of a specific crystal direction, relative to the surface normal (out-of-plane mosaicity) and relative to a particular in-plane direction (in-plane mosaicity). Crystallites that only have preferred orientation relative to the substrate surface, such as 2D powders, have exclusively out-of-plane mosaicity. By contrast, biaxially oriented films, such as epitaxially ordered films, can be evaluated based on both types of mosaicity. Pole figures enable identification of the texture type[114]. Comparison with calculated stereograms are particularly useful[128]; moreover, classical orientation distribution functions can be calculated[129].

The size or coherence length of the crystallites influences the width of the Bragg peaks (Eq. 5), explained by the specific form of the slit interference function (Fig. 1b). Thin films have limited thickness, meaning considerable peak broadening appears in the q_z direction. In principle, the same behaviour exists also in other directions (x or y direction). Larger peak broadening is present for smaller crystal extensions. With the Scherrer formula (Eq. 5)[25], the extension can be estimated taking into account the resolution limit of the set-up. Similar peak broadening results from microstrain and separation of all contributions might be possible[130–132].

An advanced analysis technique is to fully elucidate the crystal structure from the GIXD pattern. Standard single crystal approaches can be used in particular cases[133]. In general, the limited number of available Bragg peaks and the presence of many atoms in the unit cell mean that standard methods fail. As a result, a combined experimental and theoretical approach is required. The unit cell dimensions can be derived by indexing experimental data and the atom positions determined by theoretical modelling. For simple substances, the atomic positions can be guessed. For more complex substances, such as anthracene, unit cell filling by computational methods is required. Molecular dynamics simulations or density functional theory (DFT) calculations can assist; however, they require pre-knowledge, for instance the number and type of atoms involved or the chemical

structure of the molecules. Successful crystal structure solution examples are reported from thin film samples[134,135]. Both high and low symmetry crystal structures can be solved from GIXD measurements. Crystal structure solution may also be applied to 2D crystals where the intensity distribution along the Bragg rods clearly reflects the square of the structure factor $|F(q_z)|^2$ (refs. 43,44). For CTRs, the reconstruction of atoms at single crystalline surfaces can be identified[28]. However, modelling the periodic arrangements of molecules or atoms is required to analyse CTRs and 2D crystals.

Applications

GIXD is an exceptionally powerful technique for examining atomic and molecular structures across a wide range of materials, including crystalline[27,136,137] and amorphous samples[138,139]. Its versatility lies in its non-destructive nature, enabling it to be used in different sample environments, including high vacuum[94], high gas pressure[140], electrochemical set-ups[141,142] and mechanical deformation set-ups[143]. Furthermore, GIXD can be seamlessly combined with other characterization techniques, facilitating multimodal analyses. This integration opens possibilities for in situ structural characterization, including surface and interfacial reactions[53,144], thin film kinetics and dynamics[145], chemical vapour deposition[146,147] and molecular beam epitaxy[51,52,79,148]. A notable advantage of GIXD is that it can perform operando measurements, enabling real-time and real-condition correlation between structures and device performance[149–151]. To illustrate the capabilities of GIXD, this section presents several example applications, but there are many more applications. For a more extensive list of applications, please refer to the Supplementary Information.

Mechanical strains in perovskites

Some of the most intensely studied materials are perovskite-based compounds. An in-depth discussion of perovskites is available in recent reviews[45,152,153]. GIXD can be applied to quantify strain in perovskites through a careful analysis of peak positions. For instance, a study of the purely inorganic material $CsPbI_3$ (ref. 154) demonstrated how strain from the substrate–thin film interaction helps stabilize photoactive cubic or pseudo-cubic phases, known as the black phases because of their colour. These phases are obtained by quenching from elevated temperatures to room temperature, where the thermodynamically stable yellow phase is photo-inactive, non-cubic and non-perovskite. The change from the black α-phase (cubic) to β-phase (tetragonal) to γ-phase (orthorhombic) can be observed as single isotropic rings in the GIXD pattern (Fig. 5Aa). As the symmetry enhances into the cubic phase, a texture is induced that appears as arcs at different q values in the GIXD pattern. Comparing thin film GIXD data with in situ thermal X-ray diffraction data from bulk material[155], contributions to the unit cell length change could be decomposed. The change was found to result from spontaneous strain due to phase transformation, with an additional contribution from the thermal expansion coefficient mismatch between $CsPbI_3$ and the substrate. Typically, the thermal expansion coefficient for the substrate is only 10–20% of the value observed for lead halide perovskites (Fig. 5A).

Another example is a caesium-doped lead triiodide perovskite with mixed organic cations, where the cubic phase is stabilized[156] (Fig. 5B). When this material was used in solar cells, the power conversion efficiency under simulated solar illumination improved from 18.5% to 20.5% in a few hours. An in situ GIXD pattern showed isotropic rings that shifted to smaller q values in a few hours due to a light-induced lattice expansion. Analysis of the peak widths attributed the structural change to a relaxation of strain in the material from the mixed cations. The lattice expansion resulted in better alignment with the electrodes, enhancing charge extraction and reducing charge recombination, leading to the observed performance improvement.

Surface structure of oxide reconstructions

GIXD methods include CTR analysis, which relies on establishing the profile of diffraction streaks that run between the Bragg diffraction peaks (Fig. 2c). These streaks are due to the presence of a surface and show intensity modulations that are influenced by atomic ordering in the outer layers. Whereas CTRs originate from interference between X-rays scattered from the bulk and surface, fractional order rods are due to surface scattering from a reconstructed repeating unit cell with different periodicity because of atomic rearrangements at the surface. Many surface reconstructions involve complex rearrangements of multi-element materials. Often, many ordered phases can form, depending on the environment and preparation conditions. For example, oxygen vacancies can drive the reordering. Studies have focused on TiO_2, an important technological material, in different environments[157–159]. Examples include in situ X-ray diffraction under a water layer, or using the X-ray beam to drive radiolysis at a UO_2–water interface, which is important in the nuclear industry[160]. The high resolution and non-destructive nature of X-ray diffraction has enabled the structure of oxide surfaces to be studied. These structures are often difficult to investigate by other methods due to their insulating behaviour and sensitivity to damage by the probing beam, for instance, in electron diffraction.

An elegant example is presented in ref. 161, where CTR and fractional order rod measurements are used in conjunction with low-energy electron diffraction (LEED) and DFT to establish the structure of a (4 × 1) reconstruction of SnO_2(110). This correlative approach challenged the conventional idea that oxygen vacancies drive the reconstruction, by showing that it is instead based on binding of Sn_3O_3 clusters at the surface. The surface X-ray diffraction data included several in-plane reflections and fractional order rods (Fig. 6A) that originate solely from the reconstructed part of the surface. The representation of the data is given in crystal coordinates relative to the reciprocal lattice of the reconstructed surface (hkl) rather than q_x, q_y and q_z. Separating the stronger and weaker reflections, the positions of the tin atoms were initially established and refined, along with the oxygen positions, through a distortion of the hexagonal arrangement. The detailed arrangement of atoms in the reconstruction may affect the insulating behaviour of the sample, which is relevant to the gas sensing potential of tin oxide. The profile of the rods and in-plane intensities in GIXD are highly sensitive to the atomic structure. As a result, weak modulations in the CTR can establish the atomic structure and number of layers. In this case, including DFT to refine the models and LEED as an additional experiment was essential for clarifying the surface ordering.

Polymorph transitions in molecular crystals

GIXD has emerged as a highly effective technique for investigating molecular crystals at surfaces and in thin films[162,163]. Molecular crystals, which consist of 2D or 3D arrangements of molecules held together by weak intermolecular forces, exhibit unique characteristics that are essential in various fields, including electronics, optics and energy storage. GIXD experiments provide valuable diffraction patterns, offering insights into crystal lattice parameters, molecular stacking and structural changes. This information is instrumental in the design and optimization of novel devices and functional interfaces. The phenomenon

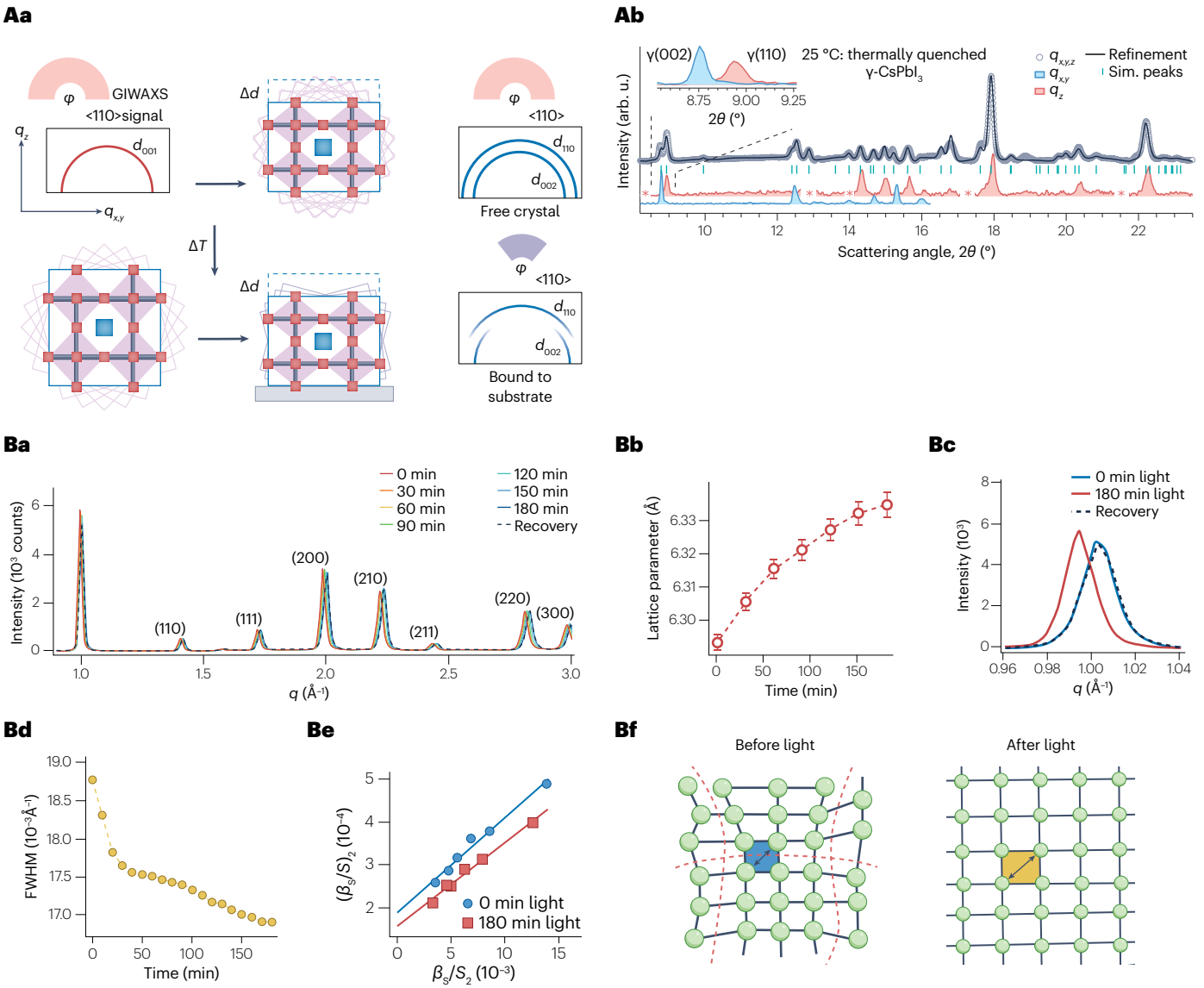

Fig. 5 | Strain effects at perovskites. A, Strain-induced stabilization of the photoactive black phases in $CsPbI_3$ films. Diffraction ring splitting in the grazing incidence X-ray diffraction (GIXD) signal. The $CsPbI_3$ lattice forms a heterojunction with the substrate surface at high temperature and undergoes tensile strain and oriented texture formation upon cooling (panel **Aa**). Integrated GIXD intensities along the q_{xy}, q_z and q_{xyz} directions of the quenched γ-$CsPbI_3$ phase show the reduction in the crystal symmetry, the emergence of the (002) and (110) peaks, from the high-symmetry cubic α-$CsPbI_3$ phase at high temperature. Lattice refinement on q_{xyz} (= q) reveals a heavy lattice distortion from the bulk γ-$CsPbI_3$ lattice, as a result of the clamping strain and rapid cooling (panel **Ab**). **B**, Light-induced lattice expansion of caesium-doped lead triiodide perovskite films with mixed organic cations. Integrated GIXD data from $FA_{0.7}MA_{0.25}Cs_{0.05}PbI_3$ (cubic phase) thin films under various illumination times and the recovery spectra display the lattice change (panel **Ba**), lattice parameter (panel **Bb**), peak intensity (panel **Bc**), peak width (panel **Bd**) and integral breadth (panel **Be**). Crystal structure change before illumination (local distortion) and after illumination (lattice expansion) (panel **Bf**). d_{hkl}, interplanar distance of the (hkl) planes; GIWAXS, grazing incidence wide-angle X-ray scattering; q_x, q_y and q_z, reciprocal space coordinates. Part **A** adapted with permission from ref. 154, PUBLISHER. Part **B** adapted with permission from ref. 156, PUBLISHER.

of polymorphism in low-dimensional n-type organic semiconductor films was recently discovered[164], and the transitions between polymorphs were mapped by GIXD. Specifically, 2D quinoidal terthiophene (2DQTT-o-B) films exhibit five distinct polymorphs, including two metastable forms and three thermally reversible forms[164] (Fig. 6B). The vertical streaked diffraction rod of polymorph III at 1.75 $Å^{-1}$ is the result of disordered layers and a signature of low-dimensional molecular packing (compared with Fig. 1c). These polymorphs show variation in charge mobility, with changes spanning five orders of magnitude, and noticeable differences in optical properties. In situ GIXD during the transition from polymorph I to polymorph II revealed a novel molecular cooperation mechanism, which is attributed to the interdigitation

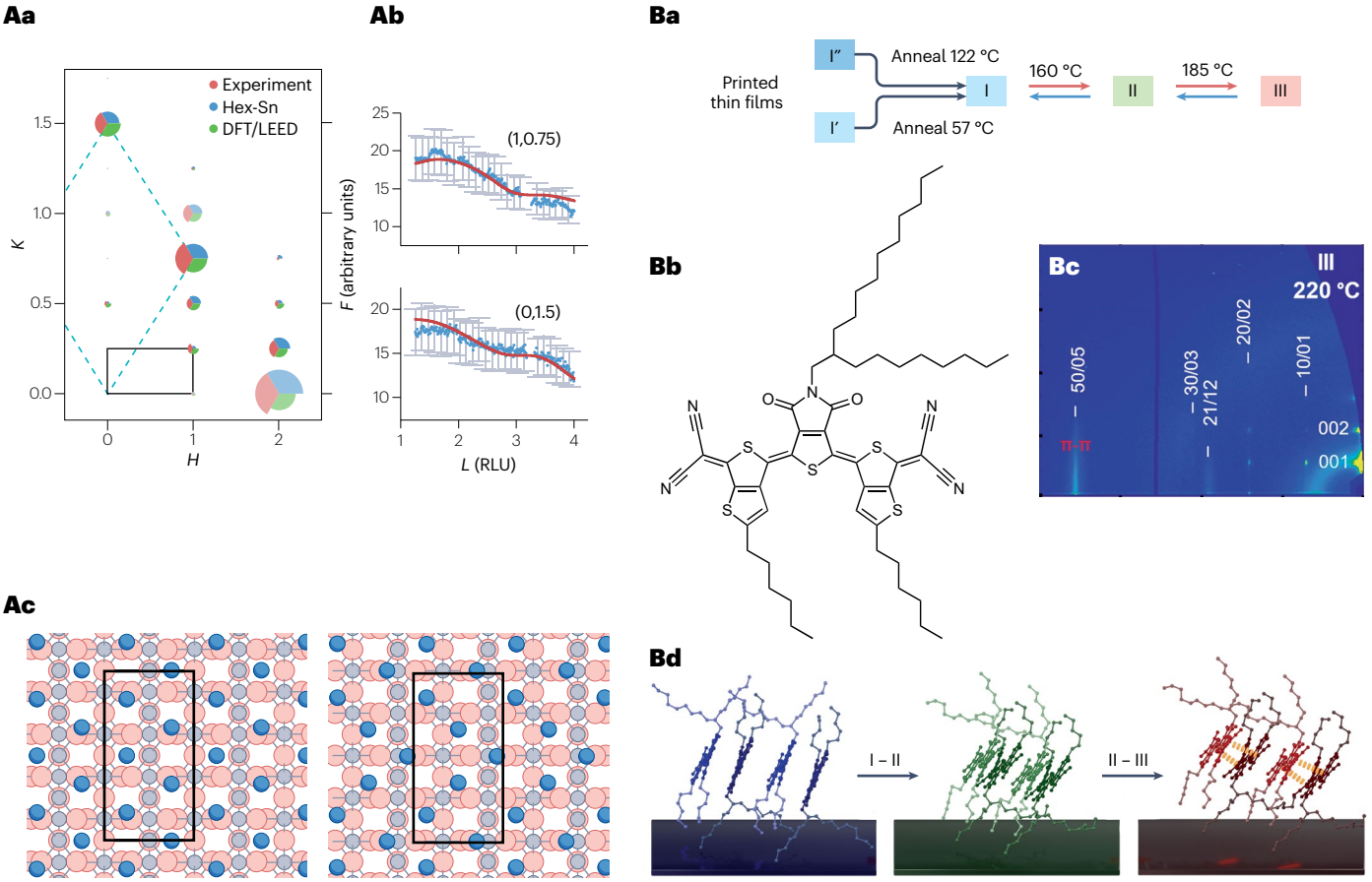

Fig. 6 | Crystal truncation rods and Bragg rods. A, Surface reconstruction at SnO_2(110) surfaces. In-plane structure factors shown as a function of the Laue index *H*, *K* and *L* = 0.5 reciprocal lattice units (panel **Aa**). Quality of the fit to the hexagonal arrangement of tin atoms towards the best-fit arrangement based around density functional theory (DFT) calculations. The best fit (red lines) is shown along two different fractional order rods (panel **Ab**). Two structural models based around a hexagonal arrangement of tin (left) and the distorted DFT based structure (right) (panel **Ac**). **B**, Polymorphism in self-assembled molecular crystal thin films. Five polymorphs of the 2D quinoidal terthiophene (2DQTT-o-B) film and their transition pathways (panel **Ba**). Molecular structure of the 2DQTT-o-B molecules (panel **Bb**). In situ grazing incidence X-ray diffraction (GIXD) pattern of polymorph III reveals a crystal structure of hexagonal unit cells together with a Bragg rod at 1.75 $Å^{-1}$. During the reversible transition from polymorph II to III, significant changes are observed in the GIXD pattern, resulting in the disappearance of numerous higher order diffraction peaks. This suggests a higher packing disorder and the formation of a higher level of symmetry compared with the transition from polymorph I to II (panel **Bc**). Proposed transition mechanisms from polymorph I to II and polymorph II to III. Conjugated cores and alkyl chains are coloured separately to improve contrast between molecules[150,151] (panel **Bd**). LEED, low-energy electron diffraction. Part **A** reprinted with permission from ref. 161, PUBLISHER. Reprinted (adapted) with permission from Davies, D. W. et al. Radically Tunable n-Type Organic Semiconductor via Polymorph Control. *Chem. Mater.* **33**, 2466–2477 (2021). Copyright {YEAR} American Chemical Society. Adapted from ref. 165, Springer Nature Limited.

of the alkyl side chains within the structure. This discovery provides insights into dynamic tuning of electronic and optical properties of 2DQTT-o-B and devices[165].

Advanced investigations

The versatility of the GIXD set-up and its ability to provide comprehensive structural information gives it broad applications, beyond the examples discussed here and in the Supplementary Information. Combining GISAXS and GIXD with multiple area detectors enables simultaneous in situ characterization of structures at various length scales with exceptional temporal resolution. This configuration has proven valuable for monitoring processes such as epitaxial growth of molecular crystals, self-assembly of nanocrystals and development of functional films for energy and catalytic applications[166–170]. The controlled penetration depth achievable with a grazing incidence geometry means that GIXD is a powerful tool for conducting residual stress depth profiling or gradient analysis on crystalline interfaces or films[171–174]. GIXD can also be integrated with high-energy X-ray total scattering and pair distribution analysis in ultra-thin films[175]. A new development uses a tomographic sequence of GIXD measurements, where spatially resolved crystallographic information is obtained with a resolution of 0.1 mm[176,177].

As next-generation synchrotron radiation sources emerge, high-coherence X-rays offer exciting opportunities. Combining high coherence with the grazing incidence geometry has the potential to

achieve near-atomic resolution in imaging structures on surfaces and thin films through coherent X-ray imaging[178]. Additionally, it may reveal hidden dynamics through X-ray photon correlation spectroscopy[179]. These developments open new avenues for advanced research and exploration in materials science and surface studies.

Reproducibility and data deposition

The reproducibility of GIXD experimental data depends strongly on the accuracy in the experimental performance. Errors can occur due to misalignment of the experimental set-up, poor calibration or changes during operation. Beam drift in synchrotrons is an additional issue. Good practice is to monitor specific parameters, such as beam flux, or to recheck the set-up by measuring a calibration standard. Reproducibility is particularly influenced by sample alignment, as grazing incidence conditions mean that the beam footprint can change considerably by small errors. Typical alignment errors include the sample surface not being located at the centre of the goniometer with respect to the desired rotation axis and translational z height; an incorrect incident angle α_i; or, in rotating GIXD, a rotation axis that is not perpendicular to the sample surface, resulting in surface wobbling[96]. Consequently, the position of diffraction peaks shifts, as depicted in Fig. 7a. As these are geometrical effects, corrections can be applied if the sample is well known. However, if unknown samples are present, this can mislead experimental outcomes. An accidental side tilt to the sample causes

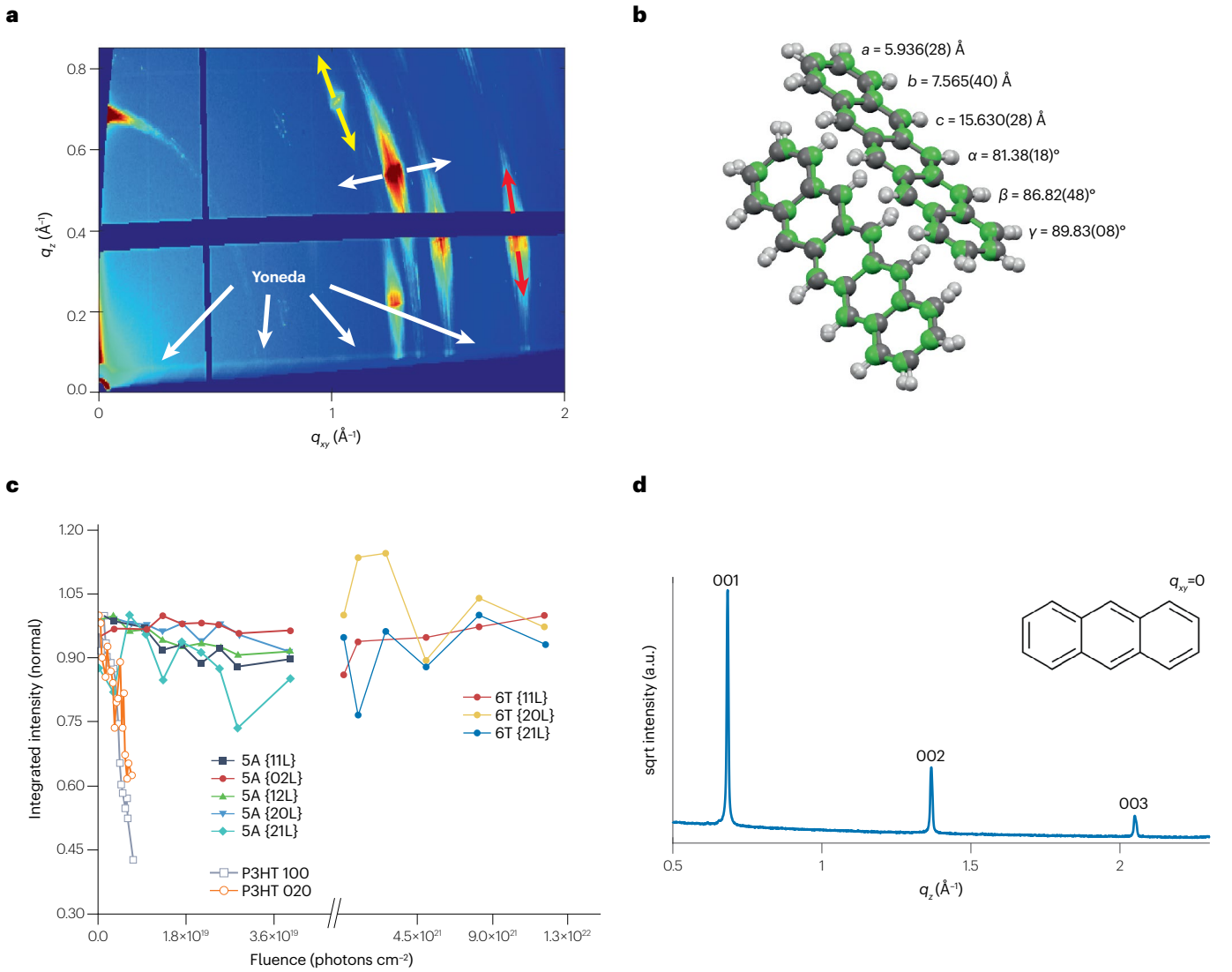

Fig. 7 | Reproducibility and limitations. a, Peak shifting due to different types of sample misalignment: error in z height (white arrows), wrong angle of grazing incidence α_i (red arrows) and misalignment in the sample rotation axis (yellow arrows). An accidental lateral tilt of the sample is visible by a non-horizontal Yoneda line. **b**, Reproducibility by comparing the crystal structure solution of pentacene (5A) in terms of lattice constants and comparison of the molecular packing. **c**, Beam damage on 5A, sexithophene (6T) and polyhexyl-thiophene (P3HT) thin films by monitoring the decrease of Bragg peak intensities[179]. **d**, Specular X-ray diffraction from a uniplanar anthracene thin film compensating the diffraction information located within the missing wedge of reciprocal space maps obtained from grazing incidence X-ray diffraction (GIXD) measurements. q_x, q_y and q_z, reciprocal space coordinates. Part **c** reprinted with permission from ref. 194, PUBLISHER.

Glossary

2D powder
(Two-dimensional powder). Crystallites with a defined crystallographic plane parallel to the substrate surface but without any azimuthal or in-plane alignment.

Angle of grazing incidence
(α_i). The angle of the primary X-ray beam relative to the sample surface is defined as the angle of incidence.

Biaxial texture
Crystallographic texture where the crystallites are preferably aligned along two different axes, for example, one perpendicular to the surface and one along a defined surface azimuth.

Bragg rods
The crystallographic lattice of two-dimensional (2D) crystals is represented by Bragg rods in the reciprocal space.

Critical angle of total external reflection
(α_c). At angles of grazing incidence below α_c, the primary X-ray beam is totally reflected from an ideally flat substrate surface.

Crystallographic texture
The distribution of crystallites within a sample in respect to their orientation relative to the sample coordinate system.

Crystal truncation rod
(CTR). Cleaving of a crystal result in a crystalline lattice with a missing half. The presence of lattice points on one side and missing lattice points on the other side results in CTRs in reciprocal space.

Macrostrain
External stress causes strain of the crystal lattice detectable by peak shifts.

Microstrain
Structural defects of crystalline lattices cause internal strain which is associated with peak broadening.

Mosaicity
Average deviation of crystal alignments (or crystal orientations) from a given sample direction.

Penetration depth
(Λ). Total reflection of the primary X-ray beam at the sample surface reduces the penetration into a sample surface to characteristic values in the nanometre range. When the angle of grazing incidence α_i is greater than the critical angle of total external reflection α_c, penetration is determined by the linear absorption coefficient μ of the sample material.

Powder plot
Integration of the measured intensity across the scattering vector $\vec{q}$, representing a diffraction pattern of randomly distributed crystallites.

Refraction correction
Only the z part of the scattering vector has to be corrected according to refraction effects; largest corrections are present at α_f and/or $\alpha_i \approx \alpha_c$, where α_f is the angle between the reflected X-ray beam and the sample surface, α_i is the angle of grazing incidence and α_c is the critical angle of total external reflection.

Scattering angles
Angles between the primary X-ray beam and the diffracted beam.

Slit interference function
General diffraction condition for gratings with a limited number of repeating units.

Wave vector
The wave vector $\vec{k}$ gives the direction of the X-ray beam; the length of the vector is related to the wavelength λ (or energy E) of the radiation.

X-ray diffraction
Superposition of coherently (and elastically) scattered X-ray waves according to their phase difference resulting from path length differences between the different scattering centres.

Yoneda peak
The scattered intensity is enhanced when the angle between the reflected X-ray beam and sample surface is close to the critical angle of total external reflection α_c.

a non-horizontal Yoneda line in the reciprocal space map (Fig. 7a), as Yoneda peaks appear experimentally at constant values of $\alpha_f = \alpha_c$[36].

The reliability of a GIXD experiment can be determined based on indexing of diffraction patterns. Lattice constants are determined by assigning Laue indices to as many individual Bragg peaks as possible. The results can be evaluated based on the uncertainties, determined by deviations between calculated and experimental peak positions[123]. Numerous examples are reported in the literature where uncertainties in the lattice constants are given[180,181].

The previous examples can be used to evaluate the quality of single diffraction patterns. However, an absolute uncertainty of GIXD experiments can be estimated only with experiments performed using different set-ups. Round robin tests give suitable information on reproducibility[182,183], but are not available for GIXD. Comparing results from popular samples offers another route. For instance, the thin film phase of pentacene (5A) was studied extensively by many groups and three different crystal structure solutions were published nearly simultaneously[184–186]. The obtained lattice constants can be compared, together with the estimated molecular packing calculated by theoretical modelling. These results are presented in Fig. 7b.

Finally, the reproducibility of GIXD experiments depends on the quality of the sample and local variation. Damage to the sample due to intense primary X-ray beams can further influence reproducibility.

Data handling

State-of-the-art GIXD experiments with high dynamic range area detectors generate large amounts of data. Variation of experimental parameters, such as in rotating GIXD or in situ experiments[187], considerably increases the amount of data, which need to be stored, handled and processed. Although technically feasible, there is currently no defined file format for GIXD data. Recent initiatives aim to address common file formats, combine experimental data with meta data and outline the requirements of repositories for processed data and data analysis portals.

Limitations and optimizations

Beam damage

In synchrotron experiments, X-ray beam-induced damage often receives insufficient attention[188]. This concern is particularly relevant when dealing with organic materials prone to damage, or during operando studies where the X-ray beam can influence the reaction under study. Beam damage primarily arises from cleavage of intramolecular and intermolecular bonds due to X-ray absorption in the sample. Additionally, radiolysis can generate reactive species, such as hydrogen gas, oxides of nitrogen or ozone, changing the sample chemistry[189]. The weak X-ray absorption in (ultra-)thin films is usually overshadowed by the impact of photoelectron production in the substrate material.

This becomes especially relevant when organics are deposited on heavier inorganic substrates, as damage caused by the cascade of secondary photoelectrons typically outweighs direct damage occurring in the delicate organic film.

To quantify beam-induced damage, it is useful to compare measurements with very short exposure times, using beam absorbers or conducting measurements on non-radiated parts by laterally translating the sample. Beam damage may present in several ways, for example, by changing the dimensions of diffraction features if long-range order is lost. Most often, however, beam damage is observed as a reduction of Bragg signals[190]. Some slight beam damage may be tolerable if the desired reflections are unaffected or if changes are understood and can be accounted for, such as by frequently scanning a standard feature to monitor changes. This can be difficult for in situ experiments where changes could be due to morphological changes in the film, or where the beam damage may be accelerated, for instance in a humid environment[45]. Some studies have focused on monitoring the morphological changes induced by beam damage[191,192], highlighting macroscopic changes that can occur under the X-ray beam. When there is limited beam damage, the overall crystal lattice might only experience minor disturbances from beam-induced defects[193,194], examples of which are shown in Fig. 7c. Strategies such as laterally translating large homogeneous samples are generally effective and ensure that measurements are consistently performed on pristine sample regions[195]. Even with optimization through translation, careful consideration of the exposure time is crucial to strike a balance between the desired signal-to-noise ratio and minimizing radiation damage to the sample. Careful selection of either the substrate material or the X-ray energy is important to reduce photoelectron production, where higher energy X-rays are generally less damaging due to lower absorption. It is also critical to ensure that the X-ray energy does not align with or closely approach the X-ray absorption edges of the substrate material. By avoiding energy ranges in the proximity of the substrate's absorption edges, the production of photoelectrons can be mitigated, preventing unwanted effects in the GIXD experiment. Alongside reducing exposure times, performing experiments at low temperatures reduces beam damage and can be used for experiments where the structure or morphology of the film is unaffected by temperature[196].

Method limitations

The grazing incidence geometry and the small number of layers in low atomic number materials — for example, organic layers — mean that the scattering strength is limited. As a result, it is particularly difficult to detect ultra-thin films, especially if they consist of randomly oriented crystallites. In these cases, a high flux of X-rays is required, as available at a synchrotron source. However, the balance between detecting a signal while avoiding beam damage is often difficult to achieve. There are some experimental considerations that can help, for instance working at or below the critical angle to enhance the scattering, but care should be taken if quantitative, intensity information is recorded at different azimuthal angles as any small misalignment or change in sample footprint can result in large changes in the detected intensity.

In many experiments, the best signal-to-noise ratio can be achieved by long integration times or by reducing background scattering. Using slits close to the sample on both the primary and diffracted beams has a major influence in reducing stray reflections. Although area detectors have revolutionized GIXD, when they are used in an open flight tube geometry there is a line of sight to many scattering points on the sample. This can lead to spurious signals or add to the angular spread of a reflection. Arrays of radial grids, referred to as Soller slits, are starting to reappear in experiments due to large improvements in the signal-to-noise ratio and advances in 3D printing that enable slits to be easily manufactured for specific resolution and detector configurations[88].

The GIXD technique and data quality strongly depend on other sample parameters, such as surface roughness, distribution of domains, degree of crystallinity and long-range order. In samples with a completely random distribution of crystallites, powder diffraction in a reflection geometry is a highly developed tool to yield information about the unit cell parameters[197]. However, if there is a preferred texture of crystallites in a polycrystalline sample, although GIXD cannot provide as much information as single crystal diffraction, it can provide valuable insights about favoured orientations and their distribution.

Equipment limitations

GIXD provides information about the structure averaged over large sample areas. The grazing incidence angles mean that a long stripe of the sample is illuminated. Although slits can select part of the sample to view, GIXD is limited in spatial resolution. This is both an advantage and a disadvantage, as many sample properties rely on the average structure whereas others depend on the small-scale sample morphology. For example, the effect of an array of grains can be indirectly inferred from the GIXD pattern but is unable to provide information on the grain distribution. Some studies have addressed this by combining GIXD with a local structural probe, such as light or electron microscopy, or a scanning technique, such as atomic force microscopy[198].

Combining GIXD with other X-ray methods — including specular diffraction, where the scattering vector lies along the surface normal — can be powerful but requires more versatile multi-axis sample and detector positioning systems. Specular X-ray diffraction can be performed on a classical goniometer by adopting a co-planar scattering geometry. This is indicated in Fig. 7d, where the specular diffraction pattern provides complementary information not accessible in the GIXD missing wedge, as shown in the example of uniplanar anthracene crystals in Fig. 4Ca. Blind spots in the GIXD pattern at the in-plane scattering vector q_x, q_y or $q_{xy} = 0$ can be further compensated using rocking curve measurements around the co-planar direction[199].

Generally, the combination of GIXD and X-ray reflectivity provides a more complete picture of the structural properties of thin films. In contrast to GIXD, X-ray reflectivity is based only on the optical reflection and transmission of the primary X-ray beam at the substrate surface[6,200]. The methods provide complementary information about the thin film structure, with crystallographic information from GIXD and layer morphology by X-ray reflectivity, including surface roughness or layer thickness.

Issues that limit GIXD can generally be overcome by careful and thoughtful experimental design. Regular monitoring of a known reflection or standard peak during experimental set-up enables the timescale of data acquisition to be identified, as well as the optimal X-ray energy, incidence angle, beam size and levels of attenuation.

Outlook

Challenges

Many GIXD studies have been undertaken, creating a body of knowledge relating the structure of materials to scattering patterns. This type of information can be used to train neural networks to relate scattering patterns to sample details, including the degree of crystallinity and the presence of strain in the layer. New methods are being created to automatically scan the published literature[201] and establish a database

of structures and patterns to predictively index and interpret scattering patterns from new materials or films[202]. For GIXD, applying these new analysis methods would open the technique to non-specialists, providing ways to correlate film morphology with other sample properties.

The level of detail that can be inferred from automated studies is likely to increase as analysis and data mining methods become more refined. For example, a network of defects or the role of grain boundaries could be linked to structural reorganization, which could be important for technological applications. As an example, the sensitivity in gas detection could be enhanced if bonding is shown to occur at defects or in low coordination sites.

Novel approaches

Most GIXD experiments at synchrotron sources use linearly polarized X-rays to enhance the scattering in the sample plane. Circularly polarized X-ray sources are also available and could be used in dichroism techniques. Small differences in the scattering strength between left and right circularly polarized light can provide information on the chirality of the film or its magnetic structure if soft X-rays are used[203]. As GIXD is a photon-in, photon-out technique, these studies are also possible under an applied magnetic field or other operando environment. If film is robust enough, other enhancements can be made by working at resonance or close to an absorption edge. Information about the structural arrangement of a specific element can be obtained, for example to identify details of induced strain in a film[204]. New high-flux, fast detectors will enable dynamic processes to be probed by direct measurement or stroboscopic methods to quantify transient changes in strain.

Diffraction-limited storage rings have enabled synchrotron X-ray beams to become increasingly coherent[205,206], resulting in novel experimental techniques that are starting to appear. For example, the average structure of a dilute assembly of nanoparticles — where the induced strain is characterized by GIXD with a large incident beam — can be linked to the structure of a single isolated particle measured by, for instance, Bragg coherent diffraction imaging. The coherence of the beam can be increased by closing the slits and focusing on scattering from a single isolated particle[207]. Other opportunities include applying X-ray photon correlation spectroscopy to understand the slow, millisecond dynamics in a film under stress, such as polymers or spin-coated films during processing[208]. The time correlation, or speckle, of the scattered intensity is recorded and interpreted with an autocorrelation function to derive the timescale of fluctuations. Faster dynamics can be accessed with methods using X-ray free electron lasers[209].

Near-term priorities

GIXD with nanometre-sized beams (nano-GIXD) has the potential to open the technique to a range of new samples[210]. Modern X-ray focusing optics, such as zone plates or capillary mirrors, can deliver high flux in beams <100 nm in diameter. Even with low grazing angles, the beam footprint is in the order of micrometres. As a result, the technique could be used to study single grains in a polycrystalline material or in a mapping modality to establish the spatial distribution of phases or strain fields. New methodologies to optimize sample alignment, ensure the beam does not move away from the grain of interest and account for thermal drift will need to be developed. New ways of interpreting the data and visualizing maps, potentially using machine learning, will also need to be established.

Efforts to automate the handling of the increasing volumes of GIXD data from the most advanced X-ray sources will benefit from the development of a standardized data format. Institutions have traditionally adopted their own standards, making cross-institute collaborations difficult. Some progress has been made with several synchrotron sources adopting the NeXus format[211]. NeXus provides a framework that would enable data analysis tools to automatically find the right data as part of a standardized workflow. More progress needs to be made in this area for the GIXD community, possibly building on the developments integrated into small-angle X-ray scattering methodologies.

Future applications

There are several future high-impact areas where GIXD will give insights into the structural origins of sample behaviour. There is a great deal of excitement about how 2D materials can be brought together, for example by transfer of exfoliated films, to form heterostructures with tailored properties[212]. The subtle structural changes that can occur when bringing together such layers, coupled through van der Waals bonding, is likely to affect other parameters such as electron transport or catalytic activity[213]. GIXD is ideally placed to provide high-resolution structural information. The ability to correlate this structural information with laboratory-based or other synchrotron techniques in the same environment, at the same time, is a research area that is likely to develop. Multi-technique studies have long been discussed and GIXD is an appropriate choice because the geometry gives relatively clear access to the sample surface for other experimental probes.

Continued improvements in detector technology, coupled with next-generation synchrotron sources, will enable GIXD to be used for faster in situ measurements. This will be important for photoluminescence, corrosion[214] and a range of energy materials, including batteries, solid oxide fuel cells[215] or perovskite solar cells[216]. The environments that samples are studied in will continue to expand, with more complex electrochemical cells and high-pressure reactors to monitor catalytic processes[54] or mechanisms for hydrogen storage. Chambers will also be developed for fine control of parameters such as heat, humidity or illumination to track their influence on the sample or film structure during growth[217] or operation. This will give insights into, for example, degradation mechanisms of photovoltaics or the long-term stability of pharmaceutical materials.

Concluding remarks

This Primer aims to provide an overview of the GIXD technique, including its origins and theoretical background, current use in state-of-the-art applications and future potential. The technique is a powerful probe of the structure of surfaces, buried interfaces and thin films and is applicable to a range of sample environments, enabling key processes to be monitored in situ, in real time and correlated with other complementary techniques. GIXD has a very bright future. It is gaining many new investigators, who are realizing the role that surfaces and interfaces play in various areas, including batteries, catalysis and novel materials. It is important that the GIXD community continues to develop analysis tools to fully exploit structural data and relate it to other techniques.

Data availability

Original data and meta data on the grazing incidence X-ray diffraction (GIXD) studies of anthracene thin films are available via the repository of the Graz University of Technology at https://doi.org/10.3217/8rxt9-jy433.

References

1. Bennett, D. W. in *Understanding Single-Crystal X-Ray Crystallography* (Wiley-VCH, 2010).
2. Clegg, W. et al. (eds) *Crystal Structure Analysis: Principles and Practice* (Oxford Univ. Press, 2009).
3. David W. I. F., Shankland K., McCusker L. B. & Bärlocher C. (eds) *Structure Determination from Powder Diffraction Data* (Oxford Univ. Press, 2006).
4. Bracco G. & Holst B. (eds) *Surface Science Techniques* (Springer, 2013).
5. Meyer, E., Bennewitz, R. & Hug, H. J. in *Scanning Probe Microscopy*. (Springer Nature, 2021).
6. Daillant, J. & Giabud, A. (eds) *X-Ray and Neutron Reflectivity* (Springer, 2009).
7. Als-Nielsen, J. & McMorrow, D. in *Elements of Modern X-ray Physics* (Wiley, 2001).
   This book gives a comprehensive overview on X-ray techniques under specific consideration of surface diffraction of X-rays.
8. Levine, J. R., Cohen, J. B., Chung, Y. W. & Georgopoulos, P. Grazing-incidence small-angle X-ray scattering: new tool for studying thin film growth. *J. Appl. Cryst.* **22**, 528–532 (1989).
9. Renaud, G., Lazzari, R. & Leroy, F. Probing surface and interface morphology with grazing incidence small angle X-ray scattering. *Surf. Sci. Rep.* **64**, 255–380 (2009).
10. Hexemer, A. & Müller-Buschbaum, P. Advanced grazing-incidence techniques for modern soft-matter materials analysis. *IUCrJ* **2**, 106–125 (2015).
11. Marra, W. C., Eisenberger, P. & Cho, A. Y. X-ray total-external-reflection–Bragg diffraction: a structural study of the GaAs–Al interface. *J. Appl. Phys.* **50**, 6927–6933 (1979).
12. Eisenberger, P. & Marra, W. C. X-ray diffraction study of the Ge(001) reconstructed surface. *Phys. Rev. Lett.* **46**, 1081–1084 (1981).
13. Pietsch, U., Holy, V. & Baumbach, T. in *High-Resolution X-Ray Scattering: From Thin Films to Lateral Nanostructures* (Springer Science & Business Media, 2004).
14. Pietsch, U. Investigations of semiconductor surfaces and interfaces by X-ray grazing incidence diffraction. *Curr. Sci.* **78**, 1484–1495 (2000).
15. Stangl, J., Holý, V. & Bauer, G. Structural properties of self-organized semiconductor nanostructures. *Rev. Mod. Phys.* **76**, 725–783 (2004).
16. Chabinyc, M. L. X-ray scattering from films of semiconducting polymers. *Polym. Rev.* **48**, 463–492 (2008).
17. Pron, A., Gawrys, P., Zagorska, M., Djurado, D. & Demadrille, R. Electroactive materials for organic electronics: preparation strategies, structural aspects and characterization techniques. *Chem. Soc. Rev.* **39**, 2577–2632 (2010).
18. Fenter, P., Schreiber, F., Zhou, L., Eisenberger, P. & Forrest, S. R. In situ studies of morphology, strain, and growth modes of a molecular organic thin film. *Phys. Rev. B* **56**, 3046–3053 (1997).
19. Banerjee, R., Kowarik, S. & Schreiber, F. in Sinha, S. K., Sanyal, M. K. & Loong, C. K. (eds.) *Advanced Characterization of Nanostructured Materials: Probing the Structure and Dynamics with Synchrotron X-rays and Neutrons* (eds Sinha, S. K., Sanyal, M. K. & Loong, C. K.) 49–95 (World Scientific, 2021).
20. Jackson, J. D. in *Classical Electrodynamics* (Wiley, 1962).
21. Sivia, D. S. in *Elementary Scattering Theory: For X-ray and Neutron Users* (Oxford Univ. Press, 2011).
22. Kittel, C. in *Introduction to Solid State Physics* (Wiley, 2004).
23. Shmueli, U. (ed.) *International Tables for Crystallography, Volume B: Reciprocal Space* (Kluwer Academic, 2006).
24. Thomas, J. I. Multiple slit interference: a hyperbola based analysis. *Eur. J. Phys.* **42**, 055304 (2021).
25. Smilgies, D.-M. Scherrer grain-size analysis adapted to grazing-incidence scattering with area detectors. *J. Appl. Cryst.* **42**, 1030–1034 (2009).
    This paper introduces the analysis of peak widths in terms of crystal size analysis.
26. Miller, A. M. et al. Extracting information from X-ray diffraction patterns containing Laue oscillations. *Z. Naturforschung B* **77**, 313–322 (2022).
27. Robinson, I. K. & Tweet, D. J. Surface X-ray diffraction. *Rep. Prog. Phys.* **55**, 599 (1992).
    This review is an easy to read, comprehensive introduction to GIXD.
28. Disa, A. S., Walker, F. J. & Ahn, C. H. High-resolution crystal truncation rod scattering: application to ultrathin layers and buried interfaces. *Adv. Mater. Interfaces* **7**, 1901772 (2020).
    This review article presents an introduction to CTRs and summarizes the achievements.
29. Savikhin, V. et al. GIWAXS-SIIRkit: scattering intensity, indexing and refraction calculation toolkit for grazing-incidence wide-angle X-ray scattering of organic materials. *J. Appl. Cryst.* **53**, 1108–1129 (2020).
30. Creagh, D. C. & Hubbell, J. H. in *International Tables for Crystallography, Volume C: Mathematical, Physical and Chemical Tables* (eds Wilson, A. J. C. & Prince, E.) (Kluwer Academic, 1999).
31. Henke, B. L., Gullikson, E. M. & Davis, J. C. X-ray interactions: photoabsorption, scattering, transmission, and reflection at E=50–30,000 eV, Z=1–92. *At. Data Nucl. Data Tables* **54**, 181–342 (1993).
32. Toney, M. F. & Brennan, S. Observation of the effect of refraction on X rays diffracted in a grazing-incidence asymmetric Bragg geometry. *Phys. Rev. B* **39**, 7963–7966 (1989).
33. Stepanov, S. A. et al. Dynamical X-ray diffraction of multilayers and superlattices: recursion matrix extension to grazing angles. *Phys. Rev. B* **57**, 4829–4841 (1998).
34. Dosch, H. Evanescent absorption in kinematic surface Bragg diffraction. *Phys. Rev. B* **35**, 2137–2143 (1987).
35. Vineyard, G. H. Grazing-incidence diffraction and the distorted-wave approximation for the study of surfaces. *Phys. Rev. B* **26**, 4146–4159 (1982).
36. Yoneda, Y. Anomalous surface reflection of X rays. *Phys. Rev.* **131**, 2010–2013 (1963).
37. Dosch, H. in *Critical Phenomena at Surfaces and Interfaces: Evanescent X-Ray and Neutron Scattering* (Springer, 1992).
38. Resel, R. et al. Multiple scattering in grazing-incidence X-ray diffraction: impact on lattice-constant determination in thin films. *J. Synchrotron Rad.* **23**, 729–734 (2016).
39. Feidenhans'l, R. Surface structure determination by X-ray diffraction. *Surf. Sci. Rep.* **10**, 105–188 (1989).
40. Reichert, H., Eng, P. J., Dosch, H. & Robinson, I. K. Thermodynamics of surface segregation profiles at Cu3Au(001) resolved by X-ray scattering. *Phys. Rev. Lett.* **74**, 2006–2009 (1995).
41. Renaud, G., Robach, O. & Barbier, A. What can we learn on the structure and morphology of metal oxide/metal interfaces by measurement of X-ray crystal truncation rods in situ, during growth. *Faraday Discuss.* **114**, 157–172 (1999).
42. Als-Nielsen, J. et al. Principles and applications of grazing incidence X-ray and neutron scattering from ordered molecular monolayers at the air–water interface. *Phys. Rep.* **246**, 251–313 (1994).
43. Kaganer, V. M., Möhwald, H. & Dutta, P. Structure and phase transitions in Langmuir monolayers. *Rev. Mod. Phys.* **71**, 779–819 (1999).
    This review gives an introduction to the field of 2D crystals at surfaces.
44. Flesch, H.-G. et al. Microstructure and phase behavior of a quinquethiophene-based self-assembled monolayer as a function of temperature. *J. Phys. Chem. C.* **115**, 22925–22930 (2011).
45. Steele, J. A. et al. How to GIWAXS: grazing incidence wide angle X-ray scattering applied to metal halide perovskite thin films. *Adv. Energy Mater.* **13**, 2300760 (2023).
46. Mahmood, A. & Wang, J.-L. A review of grazing incidence small- and wide-angle X-ray scattering techniques for exploring the film morphology of organic solar cells. *Sol. RRL* **4**, 2000337 (2020).
47. Simbrunner, J. et al. Correlation between two- and three-dimensional crystallographic lattices for epitaxial analysis. II. Experimental results. *Acta Cryst. A* **78**, 272–282 (2022).
48. Colombi, P. et al. Glancing-incidence X-ray diffraction for depth profiling of polycrystalline layers. *J. Appl. Cryst.* **39**, 176–179 (2006).
49. Robinson, I. K., Waskiewicz, W. K., Tung, R. T. & Bohr, J. Ordering at Si(111)/a-Si and Si(111)/SiO_2 interfaces. *Phys. Rev. Lett.* **57**, 2714–2717 (1986).
50. Rivnay, J., Mannsfeld, S. C. B., Miller, C. E., Salleo, A. & Toney, M. F. Quantitative determination of organic semiconductor microstructure from the molecular to device scale. *Chem. Rev.* **112**, 5488–5519 (2012).
51. Yoneda, Y. et al. Structural characterization of $BaTiO_3$ thin films grown by molecular beam epitaxy. *J. Appl. Phys.* **83**, 2458–2461 (1998).
52. Hestroffer, K. et al. In situ study of self-assembled GaN nanowires nucleation on Si(111) by plasma-assisted molecular beam epitaxy. *Appl. Phys. Lett.* **100**, 212107 (2012).
53. Lee, S. H. et al. Oxidation state and surface reconstruction of Cu under CO_2 reduction conditions from in situ X-ray characterization. *J. Am. Chem. Soc.* **143**, 588–592 (2021).
54. Martin, D. J. et al. Reversible restructuring of supported Au nanoparticles during butadiene hydrogenation revealed by operando GISAXS/GIWAXS. *Chem. Commun.* **53**, 5159–5162 (2017).
55. Neuschitzer, M. et al. Grazing-incidence in-plane X-ray diffraction on ultra-thin organic films using standard laboratory equipment. *J. Appl. Cryst.* **45**, 367–370 (2012).
56. Vegso, K. et al. A wide-angle X-ray scattering laboratory setup for tracking phase changes of thin films in a chemical vapor deposition chamber. *Rev. Sci. Instrum.* **93**, 113909 (2022).
57. Fischer, J. C. et al. GIWAXS characterization of metal–organic framework thin films and heterostructures: quantifying structure and orientation. *Adv. Mater. Interfaces* **10**, 2202259 (2023).
58. Smieska, L. et al. The functional materials beamline at CHESS. *Synchrotron Radiat. N.* **36**, 4–11 (2023).
59. Fontaine, P., Ciatto, G., Aubert, N. & Goldmann, M. Soft interfaces and resonant investigation on undulator source: a surface X-ray scattering beamline to study organic molecular films at the SOLEIL synchrotron. *Sci. Adv. Mater.* **6**, 2312–2316 (2014).
60. Takahara, A. et al. Advanced soft material beamline consortium at SPring-8 (FSBL). *Synchrotron Radiat. N.* **27**, 19–23 (2014).
61. Ogawa, H. et al. Experimental station for multiscale surface structural analyses of soft-material films at SPring-8 via a GISWAX/GIXD/XR-integrated system. *Polym. J.* **45**, 109–116 (2013).
62. Seeck, O. H. et al. The high-resolution diffraction beamline P08 at PETRA III. *J. Synchrotron Rad.* **19**, 30–38 (2012).
    This work gives a detailed description of a high-resolution GIXD set-up installed at a synchrotron source.
63. Smilgies, D.-M., Boudet, N., Struth, B. & Konovalov, O. Troika II: a versatile beamline for the study of liquid and solid interfaces. *J. Synchrotron Rad.* **12**, 329–339 (2005).
64. Bera, M. et al. Opportunities of soft materials research at advanced photon source. *Synchrotron Radiat. N.* **36**, 12–23 (2023).
65. Barbour, A. et al. X-ray scattering for soft matter research at NSLS-II. *Synchrotron Radiat. N.* **36**, 24–30 (2023).
66. Arnold, T. et al. Implementation of a beam deflection system for studies of liquid interfaces on beamline I07 at Diamond. *J. Synchrotron Rad.* **19**, 408–416 (2012).
67. Anton Paar GmbH. DHS1100: a new high-temperature attachment for materials science in the whole orientation space. *J. Appl. Cryst.* **40**, 202–202 (2007).
68. Cantelli, V. et al. The in situ growth of nanostructures on surfaces (INS) endstation of the ESRF BM32 beamline: a combined UHV–CVD and MBE reactor for in situ X-ray scattering investigations of growing nanoparticles and semiconductor nanowires. *J. Synchrotron Rad.* **22**, 688–700 (2015).

69. Ritley, K. A., Krause, B., Schreiber, F. & Dosch, H. A portable ultrahigh vacuum organic molecular beam deposition system for in situ X-ray diffraction measurements. *Rev. Sci. Instrum.* **72**, 1453–1457 (2001).
70. Kowarik, S. Thin film growth studies using time-resolved X-ray scattering. *J. Phys.: Condens. Matter* **29**, 043003 (2016).
This review gives an introduction to thin film growth studies.
71. Kneschaurek, E. et al. Compact sample environment for in situ X-ray scattering during spin-coating. *Rev. Sci. Instrum.* **94**, 063901 (2023).
72. Ruge, M., Golks, F., Zegenhagen, J., Magnussen, O. M. & Stettner, J. In operando GISAXS studies of mound coarsening in electrochemical homoepitaxy. *Phys. Rev. Lett.* **112**, 055503 (2014).
73. Festersen, S. et al. Nucleation and growth of PbBrF crystals at the liquid mercury–electrolyte interface studied by operando X-ray scattering. *Langmuir* **36**, 10905–10915 (2020).
74. Ankner, J. F., Majkrzak, C. F. & Satija, S. K. Neutron reflectivity and grazing angle diffraction. *J. Res. Natl Inst. Stand. Technol.* **98**, 47–58 (1993).
75. Kyrey, T. et al. Grazing incidence small-angle neutron scattering: background determination and optimization for soft matter samples. *Appl. Sci.* **11**, 3085 (2021).
76. Mahan, J. E., Geib, K. M., Robinson, G. Y. & Long, R. G. A review of the geometrical fundamentals of reflection high-energy electron diffraction with application to silicon surfaces. *J. Vac. Sci. Technol. A* **8**, 3692–3700 (1990).
77. Ichimiya, A. & Cohen, P. I. in *Reflection High-Energy Electron Diffraction* (Cambridge Univ. Press, 2004).
78. Hafez, M. A., Zayed, M. K. & Elsayed-Ali, H. E. Review: geometric interpretation of reflection and transmission RHEED patterns. *Micron* **159**, 103286 (2022).
79. Fumagalli, E. et al. Grazing-incidence X-ray diffraction study of rubrene epitaxial thin films. *J. Synchrotron Rad.* **19**, 682–687 (2012).
80. Renaud, G., Villette, B. & Guénard, P. Apparatus for 3D surface X-ray scattering during in situ molecular beam deposition. *Nucl. Instrum. Methods Phys. Res. Sect. B: Beam Interact. Mater. At.* **95**, 422–430 (1995).
81. Nicklin, C., Arnold, T., Rawle, J. & Warne, A. Diamond beamline I07: a beamline for surface and interface diffraction. *J. Synchrotron Rad.* **23**, 1245–1253 (2016).
82. Sakata, O. et al. Beamline for surface and interface structures at SPring-8. *Surf. Rev. Lett.* **10**, 543–547 (2003).
83. Yang, T.-Y. et al. Introduction of the X-ray diffraction beamline of SSRF. *Nucl. Sci. Tech.* **26**, 5–9 (2015).
84. Patterson, B. D. et al. The materials science beamline at the Swiss Light Source: design and realization. *Nucl. Instrum. Methods Phys. Res. Sect. A: Accelerators, Spectrometers, Detect. Associated Equip.* **540**, 42–67 (2005).
85. Patterson, B. D. et al. The materials science beamline at the Swiss Light Source. *Nucl. Instrum. Methods Phys. Res. Sect. B: Beam Interact. Mater. At.* **238**, 224–228 (2005).
86. Hexemer, A. et al. A SAXS/WAXS/GISAXS beamline with multilayer monochromator. *J. Phys.: Conf. Ser.* **247**, 012007 (2010).
87. Schlepütz, C. M. et al. Improved data acquisition in grazing-incidence X-ray scattering experiments using a pixel detector. *Acta Cryst. A* **61**, 418–425 (2005).
88. Kowarik, S. et al. A novel 3D printed radial collimator for X-ray diffraction. *Rev. Sci. Instrum.* **90**, 035102 (2019).
89. Metzger, T. H., Luidl, C., Pietsch, U. & Vierl, U. Novel versatile X-ray reflectometer for angle and energy dispersive characterization of liquid and solid surfaces and interfaces. *Nucl. Instrum. Methods Phys. Res. Sect. A: Accelerators, Spectrometers, Detect. Associated Equip.* **350**, 398–405 (1994).
90. Kowarik, S. et al. Energy-dispersive X-ray reflectivity and GID for real-time growth studies of pentacene thin films. *Thin Solid. Films* **515**, 5606–5610 (2007).
91. Wakabayashi, Y., Shirasawa, T., Voegeli, W. & Takahashi, T. Observation of structure of surfaces and interfaces by synchrotron X-ray diffraction: atomic-scale imaging and time-resolved measurements. *J. Phys. Soc. Jpn.* **87**, 061010 (2018).
92. Schlepütz, C. M., Mariager, S. O., Pauli, S. A., Feidenhans'l, R. & Willmott, P. R. Angle calculations for a (2+3)-type diffractometer: focus on area detectors. *J. Appl. Cryst.* **44**, 73–83 (2011).
93. Schwartzkopf, M. et al. Role of sputter deposition rate in tailoring nanogranular gold structures on polymer surfaces. *ACS Appl. Mater. Interfaces* **9**, 5629–5637 (2017).
94. Bertram, F., Deiter, C., Pflaum, K. & Seeck, O. H. A compact high vacuum heating chamber for in-situ X-ray scattering studies. *Rev. Sci. Instrum.* **83**, 083904 (2012).
95. Kotnik, P. et al. DHS1100—a new high temperature attachment for 4-circle X-ray goniometers. *Acta Cryst. A* **62**, 158 (2006).
96. Holzer, V. et al. Impact of sample misalignment on grazing incidence X-ray diffraction patterns and the resulting unit cell determination. *Rev. Sci. Instrum.* **93**, 063906–063906 (2022).
This paper gives the influence of sample misalignment to the diffraction pattern and introduces a procedure for sample alignment.
97. Chantler, C. T., Rae, N. A. & Tran, C. Q. Accurate determination and correction of the lattice parameter of LaB_6 (standard reference material 660) relative to that of Si(640b). *J. Appl. Cryst.* **40**, 232–240 (2007).
98. Blanton, T. N., Barnes, C. L. & Lelental, M. Preparation of silver behenate coatings to provide low- to mid-angle diffraction calibration. *J. Appl. Cryst.* **33**, 172–173 (2000).
99. Kintzel, E. J. Jr. et al. Investigation of the morphology of the initial growth of the aromatic molecule *p*-quaterphenyl on NaCl(001). *J. Vac. Sci. Technol. A* **19**, 1270–1276 (2001).
100. Roe, R. J. & Krigbaum, W. R. Description of crystallite orientation in polycrystalline materials having fiber texture. *J. Chem. Phys.* **40**, 2608–2615 (1964).
101. Heffelfinger, C. J. & Burton, R. L. X-ray determination of the crystallite orientation distributions of polyethylene terephthalate films. *J. Polym. Sci.* **47**, 289–306 (1960).
102. Mahieu, S., Ghekiere, P., Depla, D. & De Gryse, R. Biaxial alignment in sputter deposited thin films. *Thin Solid. Films* **515**, 1229–1249 (2006).
103. Hammersley, A. P. FIT2D: a multi-purpose data reduction, analysis and visualization program. *J. Appl. Cryst.* **49**, 646–652 (2016).
104. Schneider, C. A., Rasband, W. S. & Eliceiri, K. W. NIH image to ImageJ: 25 years of image analysis. *Nat. Methods* **9**, 671–675 (2012).
105. Yang, L. Using an in-vacuum CCD detector for simultaneous small- and wide-angle scattering at beamline X9. *J. Synchrotron Rad.* **20**, 211–218 (2013).
106. Kriegner, D., Wintersberger, E. & Stangl, J. xrayutilities: a versatile tool for reciprocal space conversion of scattering data recorded with linear and area detectors. *J. Appl. Cryst.* **46**, 1162–1170 (2013).
107. Jiang, Z. GIXSGUI: a MATLAB toolbox for grazing-incidence X-ray scattering data visualization and reduction, and indexing of buried three-dimensional periodic nanostructured films. *J. Appl. Cryst.* **48**, 917–926 (2015).
108. Schrode, B. et al. GIDVis: a comprehensive software tool for geometry-independent grazing-incidence X-ray diffraction data analysis and pole-figure calculations. *J. Appl. Cryst.* **52**, 683–689 (2019).
109. Klug, H. P. & Alexander, L. E. in *X-Ray Diffraction Procedures: For Polycrystalline and Amorphous Materials* (Wiley, 1974).
110. Birkholz, M. in *Thin Film Analysis by X-Ray Scattering* (Wiley-VCH, 2005).
This book summarizes the X-ray techniques for the crystallographic characterization of thin films.
111. Mason, R. The crystallography of anthracene at 95°K and 290°K. *Acta Cryst.* **17**, 547–555 (1964).
112. Baker, J. L. et al. Quantification of thin film cristallographic orientation using X-ray diffraction with an area detector. *Langmuir* **26**, 9146–9151 (2010).
113. Schulz, L. G. A direct method of determining preferred orientation of a flat reflection sample using a Geiger counter X-ray spectrometer. *J. Appl. Phys.* **20**, 1030–1033 (1949).
114. Alexander, L. E. in *X-ray Diffraction Methods in Polymer Science* (Robert E. Krieger, 1979).
115. Resel, R. et al. Wide-range three-dimensional reciprocal-space mapping: a novel approach applied to organic monodomain thin films. *J. Appl. Cryst.* **40**, 580–582 (2007).
116. Takagi, Y. & Kimura, M. Generalized grazing-incidence-angle X-ray diffraction (G-GIXD) using image plates. *J. Synchrotron Rad.* **5**, 488–490 (1998).
117. Simbrunner, J. et al. Indexing of grazing-incidence X-ray diffraction patterns: the case of fibre-textured thin films. *Acta Cryst. A* **74**, 373–387 (2018).
118. Tate, M. P. et al. Simulation and interpretation of 2D diffraction patterns from self-assembled nanostructured films at arbitrary angles of incidence: from grazing incidence (above the critical angle) to transmission perpendicular to the substrate. *J. Phys. Chem. B* **110**, 9882–9892 (2006).
119. Smilgies, D.-M. & Blasini, D. R. Indexation scheme for oriented molecular thin films studied with grazing-incidence reciprocal-space mapping. *J. Appl. Cryst.* **40**, 716–718 (2007).
120. Hinderhofer, A. et al. Machine learning for scattering data: strategies, perspectives and applications to surface scattering. *J. Appl. Cryst.* **56**, 3–11 (2023).
121. Breiby, D. W., Bunk, O., Andreasen, J. W., Lemke, H. T. & Nielsen, M. M. Simulating X-ray diffraction of textured films. *J. Appl. Cryst.* **41**, 262–271 (2008).
122. Hailey, A. K., Hiszpanski, A. M., Smilgies, D.-M. & Loo, Y.-L. The Diffraction Pattern Calculator (DPC) toolkit: a user-friendly approach to unit-cell lattice parameter identification of two-dimensional grazing-incidence wide-angle X-ray scattering data. *J. Appl. Cryst.* **47**, 2090–2099 (2014).
123. Kainz, M. P. et al. GIDInd: an automated indexing software for grazing-incidence X-ray diffraction data. *J. Appl. Cryst.* **54**, 1256–1267 (2021).
124. Talnack, F. et al. Thermal behavior and polymorphism of 2,9-didecyldinaphtho[2,3-b:2′,3′-f]thieno[3,2-b]thiophene thin films.*Mol. Syst. Des. Eng.* **7**, 507–519 (2022).
125. Smilgies, D. M. Geometry-independent intensity correction factors for grazing-incidence diffraction. *Rev. Sci. Instrum.* **73**, 1706–1710 (2002).
126. Kahn, R. et al. Macromolecular crystallography with synchrotron radiation: photographic data collection and polarization correction. *J. Appl. Cryst.* **15**, 330–337 (1982).
127. Moser, A. in *Crystal Structure Solution Based on Grazing Incidence X-Ray Diffraction* (2012).
128. Salzmann, I. & Resel, R. STEREOPOLE: software for the analysis of X-ray diffraction pole figures with IDL. *J. Appl. Cryst.* **37**, 1029–1033 (2004).
129. Pawlik, K. Determination of the orientation distribution function from pole figures in arbitrarily defined cells. *Phys. Status Solidi* **134**, 477–483 (1986).
130. Oehzelt, M. et al. Organic heteroepitaxy: *p*-sexiphenyl on uniaxially oriented α-sexithiophene. *Adv. Mater.* **18**, 2466–2470 (2006).
131. Scardi, P. et al. Size–strain separation in diffraction line profile analysis. *J. Appl. Cryst.* **51**, 831–843 (2018).
132. Nath, D., Singh, F. & Das, R. X-ray diffraction analysis by Williamson–Hall, Halder–Wagner and size–strain plot methods of CdSe nanoparticles—a comparative study. *Mater. Chem. Phys.* **239**, 122021 (2020).
133. Cantin, S., Pignat, J., Daillant, J., Perrot, F. & Konovalov, O. Grazing incidence X-ray diffraction determination of the structure of two-dimensional organic-inorganic crystals at the water surface. *Soft Matter* **6**, 1923–1932 (2010).
134. Braun, D. E. et al. Surface induced phenytoin polymorph. 1. Full structure solution by combining grazing incidence X-ray diffraction and crystal structure prediction. *Cryst. Growth Des.* **19**, 6058–6066 (2019).

Q34 Q35 Q36

135. Hao, Y. et al. From 2D to 3D: bridging self-assembled monolayers to a substrate-induced polymorph in a molecular semiconductor. *Chem. Mater.* **34**, 2238–2248 (2022).
136. Sakata, O. & Nakamura, M. in *Surface Science Techniques* (eds Bracco, G. & Holst, B.) 165–191 (Springer, 2013).
137. Simbrunner, J., Salzmann, I. & Resel, R. Indexing of grazing-incidence X-ray diffraction patterns. *Crystallogr. Rev.* **29**, 19–37 (2023).
138. Kim, G.-H. et al. High thermal conductivity in amorphous polymer blends by engineered interchain interactions. *Nat. Mater.* **14**, 295–300 (2015).
139. Proffit, D. E. et al. Thermal stability of amorphous Zn–In–Sn–O films. *J. Electroceram.* **34**, 167–174 (2015).
140. Ferrer, P., Rubio-Zuazo, J., Heyman, C., Esteban-Betegón, F. & Castro, G. R. Multi-use high/low-temperature and pressure compatible portable chamber for in situ grazing-incidence X-ray scattering studies. *J. Synchrotron Rad.* **20**, 474–481 (2013).
141. Burkle, D. et al. Development of an electrochemically integrated SR-GIXRD flow cell to study $FeCO_3$ formation kinetics. *Rev. Sci. Instrum.* **87**, 105125 (2016).
142. Scherzer, M. et al. Electrochemical surface oxidation of copper studied by in situ grazing incidence X-ray diffraction. *J. Phys. Chem. C.* **123**, 13253–13262 (2019).
143. Lee, M. Y. et al. Regular H-bonding-containing polymers with stretchability up to 100% external strain for self-healable plastic transistors. *Chem. Mater.* **32**, 1914–1924 (2020).
144. Zhu, W. et al. Kinetically controlled growth of sub-millimeter 2D Cs_2SnI_6 nanosheets at the liquid–liquid interface. *Small* **17**, 2006279 (2021).
145. Greco, A. et al. Kinetics of ion-exchange reactions in hybrid organic–inorganic perovskite thin films studied by in situ real-time X-ray scattering. *J. Phys. Chem. Lett.* **9**, 6750–6754 (2018).
146. Ranacher, C. et al. Layered nanostructures in proton conductive polymers obtained by initiated chemical vapor deposition. *Macromolecules* **48**, 6177–6185 (2015).
147. Perrotta, A., Christian, P., Jones, A. O. F., Muralter, F. & Coclite, A. M. Growth regimes of poly(perfluorodecyl acrylate) thin films by initiated chemical vapor deposition. *Macromolecules* **51**, 5694–5703 (2018).
148. Cohin, Y. et al. Growth of vertical GaAs nanowires on an amorphous substrate via a fiber-textured Si platform. *Nano Lett.* **13**, 2743–2747 (2013).
149. Huss-Hansen, M. K. et al. Structural stability of naphthyl end-capped oligothiophenes in organic field-effect transistors measured by grazing-incidence X-ray diffraction in operando. *Org. Electron.* **49**, 375–381 (2017).
150. Paulsen, B. D. et al. Time-resolved structural kinetics of an organic mixed ionic–electronic conductor. *Adv. Mater.* **32**, 2003404 (2020).
151. Qiao, Y. et al. Mechanistic insights into aldehyde production from electrochemical CO_2 reduction on CuAg alloy via operando X-ray measurements. *ACS Catal.* **13**, 9379–9391 (2023).
152. Qin, M., Chan, P. F. & Lu, X. A systematic review of metal halide perovskite crystallization and film formation mechanism unveiled by in situ GIWAXS. *Adv. Mater.* **33**, 2105290 (2021).
153. Tan, W. L. & McNeill, C. R. X-ray diffraction of photovoltaic perovskites: principles and applications. *Appl. Phys. Rev.* **9**, 021310 (2022).
154. Steele, J. A. et al. Thermal unequilibrium of strained black $CsPbI_3$ thin films. *Science* **365**, 679–684 (2019).
This recent review gives a comprehensive introduction to GIXD investigations for thin films with uniplanar texture.
155. Marronnier, A. et al. Anharmonicity and disorder in the black phases of cesium lead iodide used for stable inorganic perovskite solar cells. *ACS Nano* **12**, 3477–3486 (2018).
156. Tsai, H. et al. Light-induced lattice expansion leads to high-efficiency perovskite solar cells. *Science* **360**, 67–70 (2018).
This paper introduces a method to obtain spatial resolved crystallographic information from GIXD performed in a tomographic mode.
157. Treacy, J. P. W. et al. Structure of a superhydrophilic surface: wet chemically prepared rutile-TiO_2(110)(1×1). *J. Phys. Chem. C.* **123**, 8463–8468 (2019).
158. Hussain, H. et al. Water-induced reversal of the TiO_2(011)-(2×1) surface reconstruction: observed with in situ surface X-ray diffraction. *J. Phys. Chem. C.* **123**, 13545–13550 (2019).
159. Nadeem, I. M. et al. Water dissociates at the aqueous interface with reduced anatase TiO_2(101). *J. Phys. Chem. Lett.* **9**, 3131–3136 (2018).
160. Springell, R. et al. Water corrosion of spent nuclear fuel: radiolysis driven dissolution at the UO_2/water interface. *Faraday Discuss.* **180**, 301–311 (2015).
161. Merte, L. R. et al. Structure of the SnO_2(110)-(4×1) surface. *Phys. Rev. Lett.* **119**, 096102 (2017).
162. Novák, J. et al. Crystal growth of para-sexiphenyl on clean and oxygen reconstructed Cu(110) surfaces. *Phys. Chem. Chem. Phys.* **13**, 14675–14684 (2011).
163. Jones, A. O. F., Chattopadhyay, B., Geerts, Y. H. & Resel, R. Substrate-induced and thin-film phases: polymorphism of organic materials on surfaces. *Adv. Funct. Mater.* **26**, 2233–2255 (2016).
164. Davies, D. W. et al. Radically tunable n-type organic semiconductor via polymorph control. *Chem. Mater.* **33**, 2466–2477 (2021).
165. Davies, D. W. et al. Unraveling two distinct polymorph transition mechanisms in one n-type single crystal for dynamic electronics. *Nat. Commun.* **14**, 1304 (2023).
166. Wu, W.-R. et al. Competition between fullerene aggregation and poly(3-hexylthiophene) crystallization upon annealing of bulk heterojunction solar cells. *ACS Nano* **5**, 6233–6243 (2011).
167. Huang, Y.-C. et al. Insight into evolution, processing and performance of multi-length-scale structures in planar heterojunction perovskite solar cells. *Sci. Rep.* **5**, 13657 (2015).
168. Weidman, M. C., Smilgies, D.-M. & Tisdale, W. A. Kinetics of the self-assembly of nanocrystal superlattices measured by real-time in situ X-ray scattering. *Nat. Mater.* **15**, 775–781 (2016).
169. Hodas, M. et al. Real-time monitoring of growth and orientational alignment of pentacene on epitaxial graphene for organic electronics. *ACS Appl. Nano Mater.* **1**, 2819–2826 (2018).
170. Vakalopoulou, E. et al. Metal sulfide thin films with tunable nanoporosity for photocatalytic applications. *ACS Appl. Nano Mater.* **5**, 1508–1520 (2022).
171. Predecki, P., Zhu, X. & Ballard, B. Proposed methods for depth profiling of residual stresses using grazing incidence X-ray diffraction (GIXD). *Adv. X-Ray Anal.* **36**, 237–245 (1992).
172. Angerer, P. & Strobl, S. Equi-penetration grazing incidence X-ray diffraction method: stress depth profiling of ground silicon nitride. *Acta Mater.* **77**, 370–378 (2014).
173. Wang, H. et al. Interfacial residual stress relaxation in perovskite solar cells with improved stability. *Adv. Mater.* **31**, 1904408 (2019).
174. Yazdanmehr, A. & Jahed, H. On the surface residual stress measurement in magnesium alloys using X-ray diffraction. *Materials* **13**, 5190 (2020).
175. Dippel, A.-C. et al. Local atomic structure of thin and ultrathin films via rapid high-energy X-ray total scattering at grazing incidence. *IUCrJ* **6**, 290–298 (2019).
176. Tsai, E. H. R., Xia, Y., Fukuto, M., Loo, Y.-L. & Li, R. Grazing-incidence X-ray diffraction tomography for characterizing organic thin films. *J. Appl. Cryst.* **54**, 1327–1339 (2021).
177. Smilgies, D.-M., Koker, M. K. A., Li, R., Shaw, L. & Bao, Z. Grazing-incidence texture tomography and diffuse reflectivity tomography of an organic semiconductor device array. *Chemistry–Methods* **2**, e202200016 (2022).
178. Miao, J., Ishikawa, T., Robinson, I. K. & Murnane, M. M. Beyond crystallography: diffractive imaging using coherent X-ray light sources. *Science* **348**, 530–535 (2015).
179. Sandy, A. R., Zhang, Q. & Lurio, L. B. Hard X-ray photon correlation spectroscopy methods for materials studies. *Annu. Rev. Mater. Res.* **48**, 167–190 (2018).
180. Kowarik, S. et al. Real-time X-ray diffraction measurements of structural dynamics and polymorphism in diindenoperylene growth. *Appl. Phys. A* **95**, 233–239 (2009).
181. Simbrunner, J. et al. Indexing grazing-incidence X-ray diffraction patterns of thin films: lattices of higher symmetry. *J. Appl. Cryst.* **52**, 428–439 (2019).
182. Unterumsberger, R. et al. A round robin test for total reflection X-ray fluorescence analysis using preselected and well characterized samples. *J. Anal. At. Spectrom.* **36**, 1933–1945 (2021).
183. Colombi, P. et al. Reproducibility in X-ray reflectometry: results from the first world-wide round-robin experiment. *J. Appl. Cryst.* **41**, 143–152 (2008).
184. Schiefer, S., Huth, M., Dobrinevski, A. & Nickel, B. Determination of the crystal structure of substrate-induced pentacene polymorphs in fiber structured thin films. *J. Am. Chem. Soc.* **129**, 10316–10317 (2007).
185. Yoshida, H., Inaba, K. & Sato, N. X-ray diffraction reciprocal space mapping study of the thin film phase of pentacene. *Appl. Phys. Lett.* **90**, 181930 (2007).
186. Nabok, D. et al. Crystal and electronic structures of pentacene thin films from grazing-incidence X-ray diffraction and first-principles calculations. *Phys. Rev. B* **76**, 235322 (2007).
187. Gründer, Y., Stettner, J. & Magnussen, O. M. Review—in-situ surface X-ray diffraction studies of copper electrodes: atomic-scale interface structure and growth behavior. *J. Electrochem. Soc.* **166**, D3049 (2018).
188. Holton, J. M. A beginner's guide to radiation damage. *J. Synchrotron Rad.* **16**, 133–142 (2009).
189. Meents, A., Gutmann, S., Wagner, A. & Schulze-Briese, C. Origin and temperature dependence of radiation damage in biological samples at cryogenic temperatures. *Proc. Natl Acad. Sci. USA* **107**, 1094–1099 (2010).
190. Davies, R. J., Burghammer, M. & Riekel, C. Micro-Raman spectroscopy as an in situ tool for probing radiation damage during microdiffraction experiments in soft condensed matter. *Macromolecules* **41**, 7251–7253 (2008).
191. Antonio, E. N. & Toney, M. F. Why it is important to determine and report the impact of probe radiation. *Joule* **6**, 723–725 (2022).
192. Li, M. et al. Evidence of morphological change in sulfur cathodes upon irradiation by synchrotron X-rays. *ACS Energy Lett.* **7**, 577–582 (2022).
193. Meents, A., Dittrich, B. & Gutmann, S. A new aspect of specific radiation damage: hydrogen abstraction from organic molecules. *J. Synchrotron Rad.* **16**, 183–190 (2009).
194. Neuhold, A. et al. X-ray radiation damage of organic semiconductor thin films during grazing incidence diffraction experiments. *Nucl. Instrum. Methods Phys. Res. Sect. B: Beam Interact. Mater. At.* **284**, 64–68 (2012).
195. Stenger, P. C. et al. X-ray diffraction and reflectivity validation of the depletion attraction in the competitive adsorption of lung surfactant and albumin. *Biophys. J.* **97**, 777–786 (2009).
196. Warkentin, M. & Thorne, R. E. Glass transition in thaumatin crystals revealed through temperature-dependent radiation-sensitivity measurements. *Acta Cryst. D.* **66**, 1092–1100 (2010).
197. Kaduk, J. A. et al. Powder diffraction. *Nat. Rev. Methods Primers* **1**, 1–22 (2021).
198. Yang, H. et al. Conducting AFM and 2D GIXD studies on pentacene thin films. *J. Am. Chem. Soc.* **127**, 11542–11543 (2005).
199. Pachmajer, S., Werzer, O., Mennucci, C., Buatier de Mongeot, F. & Resel, R. Biaxial growth of pentacene on rippled silica surfaces studied by rotating grazing incidence X-ray diffraction. *J. Cryst. Growth* **519**, 69–76 (2019).
200. Tolan, M. *X-Ray Scattering from Soft-Matter Thin Films* 148 (Springer, 1999).
This book introduces X-ray reflectivity which is often used as a supplementary X-ray technique to characterize surfaces, interfaces and thin films.
201. Swain, M. C. & Cole, J. M. ChemDataExtractor: a toolkit for automated extraction of chemical information from the scientific literature. *J. Chem. Inf. Model.* **56**, 1894–1904 (2016).

202. Olivetti, E. A. et al. Data-driven materials research enabled by natural language processing and information extraction. *Appl. Phys. Rev.* **7**, 041317 (2020).
Q37
203. Steadman, P. & Fan, R. in *Hyperspectral Imaging—A Perspective on Recent Advances and Applications* (IntechOpen, 2022).
204. Chamard, V. et al. Anomalous diffraction in grazing incidence to study the strain induced by GaN quantum dots stacked in an AlN multilayer. *Nucl. Instrum. Methods Phys. Res. Sect. B: Beam Interact. Mater. At.* **200**, 95–99 (2003).
205. Eriksson, M., van der Veen, J. F. & Quitmann, C. Diffraction-limited storage rings—a window to the science of tomorrow. *J. Synchrotron Rad.* **21**, 837–842 (2014).
206. Raimondi, P. & Liuzzo, S. M. Toward a diffraction limited light source. *Phys. Rev. Accel. Beams* **26**, 021601 (2023).
207. Estandarte, A. K. C. et al. Bragg coherent diffraction imaging of iron diffusion into gold nanocrystals. *N. J. Phys.* **20**, 113026 (2018).
208. Sinha, S. K., Jiang, Z. & Lurio, L. B. X-ray photon correlation spectroscopy studies of surfaces and thin films. *Adv. Mater.* **26**, 7764–7785 (2014).
209. Dallari, F. et al. Analysis strategies for MHz XPCS at the European XFEL. *Appl. Sci.* **11**, 8037 (2021).
210. Stangl, J., Mocuta, C., Chamard, V. & Carbone, D. in *Nanobeam X-Ray Scattering: Probing Matter at the Nanoscale* (Wiley-VCH, 2013).
211. Könnecke, M. et al. The NeXus data format. *J. Appl. Cryst.* **48**, 301–305 (2015).
212. Zielinski, P. et al. Probing exfoliated graphene layers and their lithiation with microfocused X-rays. *Nano Lett.* **19**, 3634–3640 (2019).
213. Sonntag, J. et al. Excellent electronic transport in heterostructures of graphene and monoisotopic boron-nitride grown at atmospheric pressure. *2D Mater.* **7**, 031009 (2020).
214. Joshi, G. R. et al. in *NACE CORROSION* (OnePetro, 2015).
215. Pramana, S. S. et al. Understanding surface structure and chemistry of single crystal lanthanum aluminate. *Sci. Rep.* **7**, 43721 (2017).
216. Alhazmi, N., Pineda, E., Rawle, J., Howse, J. R. & Dunbar, A. D. F. Perovskite crystallization dynamics during spin-casting: an in situ wide-angle X-ray scattering study. *ACS Appl. Energy Mater.* **3**, 6155–6164 (2020).
217. Nicklin, C. et al. MINERVA: a facility to study microstructure and interface evolution in realtime under vacuum. *Rev. Sci. Instrum.* **88**, 103901 (2017).

Acknowledgements
The authors thank beamline XRD1, synchrotron Elettra and Trieste for providing beamtime to perform grazing incidence X-ray diffraction (GIXD) measurements to show different types of anthracene thin films. Argonne National Laboratory's work was supported by the US Department of Energy, Office of Science, under contract DE-AC02-06CH11357.

Author contributions
Introduction (R.R.); Experimentation (S.K.); Results (O.W., F.G.); Applications (Z.J., J.S.); Reproducibility and data deposition (R.R.); Limitations and optimizations (C.N.); Outlook (C.N.); Overview of the Primer (all authors).

Competing interests
The authors declare no competing interests.

Additional information
Supplementary information The online version contains supplementary material available at https://doi.org/10.1038/s43586-024-00293-8.

Peer review information *Nature Reviews Methods Primers* thanks Marianna Marciszko and the other, anonymous, reviewer(s) for their contribution to the peer review of this work.

QUERY FORM

Manuscript ID	
Author	

AUTHOR:

The following queries have arisen during the editing of your manuscript. Please answer by making the requisite corrections directly in the e.proofing tool rather than marking them up on the PDF. This will ensure that your corrections are incorporated accurately and that your paper is published as quickly as possible.

Query No.	*Nature of Query*
Q1:	Please provide department for affiliation 1
Q2:	Please check your article carefully, coordinate with any co-authors and enter all final edits clearly in the eproof, remembering to save frequently. Once corrections are submitted, we cannot routinely make further changes to the article.
Q3:	Note that the eproof should be amended in only one browser window at any one time; otherwise changes will be overwritten.
Q4:	Author surnames have been highlighted. Please check these carefully and adjust if the first name or surname is marked up incorrectly, as this will affect indexing of your article in public repositories such as PubMed. Also, carefully check the spelling and numbering of all author names and affiliations, and the corresponding author(s) email address(es). Please note that email addresses should only be included for designated corresponding authors, and you cannot change corresponding authors at this stage except to correct errors made during typesetting.
Q5:	You cannot alter accepted Supplementary Information files except for critical changes to scientific content. If you do resupply any files, please also provide a brief (but complete) list of changes. If these are not considered scientific changes, any altered Supplementary files will not be used, only the originally accepted version will be published.
Q6:	Please note subscripts are presented in Roman unless they are variables. If any subscripts are variables and incorrectly presented, please change to italics
Q7:	Please confirm "e" is exponential factor in Eq. 4, or italicize and define if a variable
Q8:	Please confirm that the edits to the sentence 'Typically, δ ranges ….' preserve the originally intended meaning.
Q9:	Please confirm consistent use of variable "α_c" with lowercase c is correct throughout, or provide revisions

QUERY FORM

Manuscript ID	
Author	

AUTHOR:

The following queries have arisen during the editing of your manuscript. Please answer by making the requisite corrections directly in the e.proofing tool rather than marking them up on the PDF. This will ensure that your corrections are incorporated accurately and that your paper is published as quickly as possible.

Query No.	*Nature of Query*
Q10:	Please confirm that the edits to the sentence 'This enhancement is due ....' preserve the originally intended meaning.
Q11:	Please confirm that the edits to the sentence 'Using GIXD, analysis....' preserve the originally intended meaning.
Q12:	Please confirm that the edits to the sentence 'Using intense synchrotron ....' preserve the originally intended meaning.
Q13:	Please ensure θ_f and θ_i are defined at first citation in text and figure captions
Q14:	Please confirm "rotates along θ_i", or change to "rotates around θ_i"
Q15:	The Figure 4 call-outs have been updated to reflect the new lettering system. Please double check that all panels are called out correctly.
Q16:	Please provide all missing text after "results in intensity variations along the"
Q17:	Please confirm change to "red dots" in Fig. 4Cc caption to match image, or provide revisions
Q18:	Please clarify the 5 uses of "along sphere...", "along the ring...", "along concentric circle..." in this section - should 'along' be replaced by "around"?
Q19:	Please confirm that the edits to the sentence 'The change from ....' preserve the originally intended meaning.
Q20:	Please confirm inserted definitions and define φ and β^S/S in Fig. 5 caption, confirming βS/S axes labels are correct in image
Q21:	Please confirm use of capitals is correct for "Laue indices *H*, *K* and *L*" in Fig. 6, but *h,k,l* is used throughout the rest of the article

QUERY FORM

Manuscript ID	
Author	

AUTHOR:

The following queries have arisen during the editing of your manuscript. Please answer by making the requisite corrections directly in the e.proofing tool rather than marking them up on the PDF. This will ensure that your corrections are incorporated accurately and that your paper is published as quickly as possible.

Query No.	*Nature of Query*
Q22:	Please confirm that the edits to the Fig. 6 caption sentence 'Proposed transition mechanisms....' preserve the originally intended meaning.
Q23:	Please confirm that the edits to the sentence 'Although technically ....' preserve the originally intended meaning.
Q24:	Please confirm that the edits to the sentence 'Arrays of radial ....' preserve the originally intended meaning.
Q25:	Please confirm that the edits to the sentence 'This is both an advantage ....' preserve the originally intended meaning.
Q26:	Please confirm changes to "NeXus" are OK
Q27:	Please confirm that the edits to the Glossary entry 'Wave vector' are OK
Q28:	Please confirm updated page span for reference 95, 125
Q29:	Please provide names and initials of editors and page span for reference 1, 5, 7, 13
Q30:	Please confirm details are correct and complete for reference 2, 3, 4, 6
Q31:	Please provide names and initials of editors and page span for reference 20, 21, 22
Q32:	Please provide page span for reference 30
Q33:	Please provide names and initials of editors and page span for reference 37
Q34:	Please provide names and initials of editors and page span for reference 77
Q35:	Please provide names and initials of editors and page span for reference 109, 110, 114

QUERY FORM

Manuscript ID	
Author	

AUTHOR:

The following queries have arisen during the editing of your manuscript. Please answer by making the requisite corrections directly in the e.proofing tool rather than marking them up on the PDF. This will ensure that your corrections are incorporated accurately and that your paper is published as quickly as possible.

Query No.	*Nature of Query*
Q36:	Please provide names and initials of editors, page span and publisher for reference 127
Q37:	Please provide names and initials of editors and page span for reference 203, 210, 214